EFFECTS OF NANOCRYSTALLINE SILICON INCLUSIONS IN DOPED AND

UNDOPED THIN FILMS OF HYDROGENATED AMORPHOUS SILICON

A DISSERTATION

SUBMITTED TO THE FACULTY OF THE GRADUATE SCHOOL

OF THE UNIVERSITY OF MINNESOTA

BY

CHARLIE PEARMAN BLACKWELL

IN PARTIAL FULFILLMENT OF THE REQUIREMENTS

FOR THE DEGREE OF

DOCTOR OF PHILOSOPHY

JAMES KAKALIOS

DECEMBER 2009

Acknowledgements

First of all, I have to give many thanks to my advisor Prof. Jim Kakalios for his patience and teaching style throughout my time as his research assistant. No matter how well or how unpredictable my results were he consistently finished the meeting with the words, "Get Back to Work". I would also like to thank the members of the oral defense exam committee: Uwe Kortshagen (co-advisor), E. Dan Dahlberg, Charles Campbell, and Bob Lysak (preliminary exam). I must also give thanks to my family back home in Georgia that continued to encourage me to excel in my education from the time that I was on the Principal's List in elementary school. Mary Diallo Ph.D., my aunt, has also been a necessary factor in my life. When looking at which undergraduate institution to enroll into she introduced me to Mrs. Dedra Azonobi-O' Neal, Prof. Joseph Johnson III, and Dr. Lynette Johnson who were all instrumental in me being able to attend Florida Agricultural and Mechanical University. During the first day orientation for Life-Gets-Better Scholarship, Mrs. Azonobi-O'Neal set the expectation that each of us would go on to graduate school. I must also thank Prof. Joseph Johnson III and Dr. Lynette Johnson for their constant mentoring while I interned in the research lab my freshman, sophomore, and junior years.

I would also like to acknowledge Prof. Frank Snowden who had me work as an intern in the Materials Research Science and Engineering Center and was a constant mentor and supporter during my time at the University of Minnesota. Many thanks to Jim Belich for the introduction into various measurements performed in the lab, Siri

Dedication

I dedicate this thesis to my family, friends, mentors, and everyone else who encouraged

me with the words, "You can do it."

Abstract

Hydrogenated amorphous silicon has attracted considerable interest as a low-cost

material for various large-area electronic devices, such as scanners, thin film transistors

employed in flat panel displays, and photovoltaic devices. A major limitation of

amorphous silicon is a light-induced degradation of the photoconductivity and dark

conductivity, associated with the creation of metastable dangling bond defects. Recent

reports that mixed phase thin films, consisting of silicon nanocrystallites embedded

within a hydrogenated amorphous silicon matrix, display a resistance to this light-induced

degradation have motivated the development of a novel deposition system to synthesize

such materials. Conventional techniques to generate such amorphous/nanocrystalline

mixed phase films involve running a Plasma Enhanced Chemical Vapor Deposition

system very far from those conditions that yield high quality amorphous silicon. A dual-

plasma co-deposition system has thus been constructed, whereby the silicon nanoparticles

can be fabricated in one chamber, and then injected into a second plasma reactor, in

which the surrounding amorphous silicon is deposited. The deposition process, as well as

structural, optical, and electronic characterization of these films, including the dark

conductivity, photoconductivity, infra-red absorption spectra, micro-RAMAN spectra,

and the optical absorption spectra, will be discussed for these films.

Table of Contents   Page

Table of Contents   Page

List of Tables   Page

List of Figures   Page

List of Figures   Page

List of Figures   Page

List of Figures

Page

List of Figures   Page

List of Figures   Page

List of Figures   Page

List of Figures   Page

1.- Introduction

The ability to easily dope crystalline silicon either negatively or positively by the addition of a small concentration of impurities has made it the material of choice for many electronics applications. Despite its abundance and versatility, single crystalline silicon has drawbacks for certain applications, such as photovoltaics or image processing, that require non-brittle, large area, thin film semiconductors. Consequently there is considerable interest in using amorphous silicon for these applications due to the ease and low cost of producing thin films over large areas. These advantages can, in certain circumstances, outweigh the lower conductivity and solar conversion efficiency of amorphous silicon compared to single crystalline materials. The deposition technique most commonly used to synthesize thin film amorphous silicon is plasma enhanced chemical vapor deposition (PECVD). Materials deposited in this way contain approximately 10 at. % hydrogen covalently bonded in the amorphous network, and hydrogenated amorphous silicon (a-Si:H) can be more properly considered an alloy of silicon and hydrogen. The bonded hydrogen passivates many pre-existing dangling bond defects, and also relieves strain in the silicon network. Hydrogenated amorphous silicon is thus the predominant semiconductor for many large area opto-electronics applications and consequently the research described in this dissertation will be exclusively with the properties of a-Si:H.

1.a.- Background

Whether a material is a metal or an insulator is reflected in the location of the Fermi energy – those materials where the Fermi energy resides within a partially occupied band are metallic, while insulators are those materials for which the Fermi energy lies within the gap between the highest occupied energy band and the lowest unoccupied energy band, as sketched in Figure 1. The distinction between semiconductors and insulators is more subjective and is related to the magnitude of the energy gap separating the occupied and unoccupied bands. If this energy gap is less than approximately 3 eV, then the material is considered a semiconductor. In this case at room temperature there is typically a significant density of thermally excited charge carriers to provide a measureable dark conductivity, and photons in the near uv-visible portion of the electromagnetic spectrum are energetic enough to generate a photocurrent.

Solid state physics predominately focuses on the study of crystalline materials that are assumed to be perfectly periodic. The uniform long-range order of perfect crystals supports the application of Bloch's Theorem, and provides solutions for the bulk opto-electronic and structural properties of the solid. At the other extreme of perfectly ordered systems are completely random systems that are in thermodynamic equilibrium, such as a gas. In this case the system is equally likely to be found in any of the states accessible to it, and one may apply statistical mechanical techniques to describe the material's bulk properties. Structurally complicated amorphous materials, as indicated in

Figure 2, such as melt-quenched glass or plasma deposited amorphous silicon, lack the long range order found in crystalline materials, nor are they in thermodynamic equilibrium, a prerequisite for statistical mechanical treatments, complicating descriptions of their bulk properties based upon an understanding of their atomic constituents.

While the transport properties of crystalline silicon lead to superior performance in many electronic applications, this material is relatively expensive and difficult to produce over large areas as a thin film. One commonly used process for synthesizing single crystal silicon involves slowly drawing a crystal seed from molten silicon, generating a boule of silicon that solidifies following the seed crystal's orientations. The cylinder of single crystal silicon is then repeatedly zone-refined, and finally sliced into very thin wafers followed by polishing, all while keeping the defect density as low as possible. N-type and P-type regions, and insulating oxides and electrodes are then added to create integrated circuits and microchips from these crystalline silicon wafers. For many large area applications, such as solar panels, thin film transistors for flat panel displays, scanners or medical x-ray recording devices, a large cylinder or relatively thick (on the order of millimeters) wafer of restricted diameter is not viable.[1-3] The ability to deposit hydrogenated amorphous silicon, doped n-type, p-type, or compensated, as a thin film (less than one micron in thickness) over nearly arbitrarily large areas on a wide variety of substrate surfaces has generated much interest in understanding and optimizing this material's opto-electronic properties.[4-6]
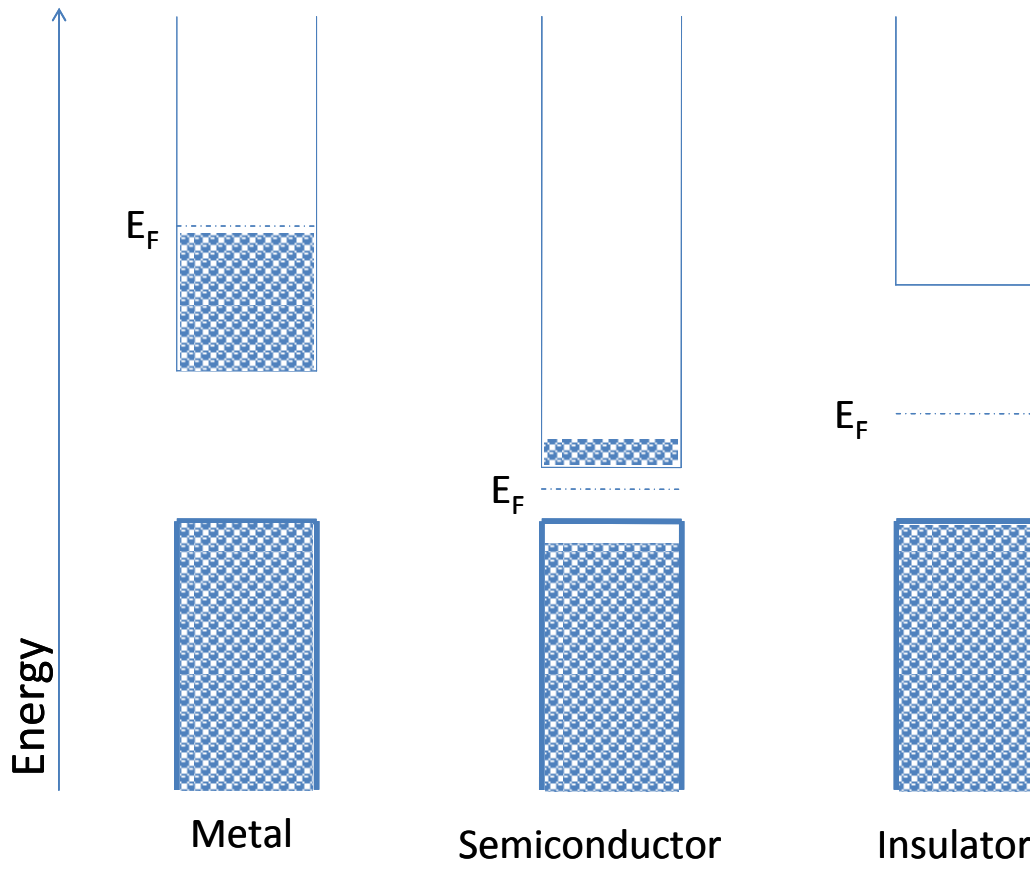
Figure 1. Energy diagrams of three types of materials, where the valence band is denoted by a bold, solid line, the conduction band within a solid line, and the Fermi energy is indicated with a dashed line.

Crystalline Silicon
Ordered

Gas
Random

Amorphous Silicon
Dis - Ordered
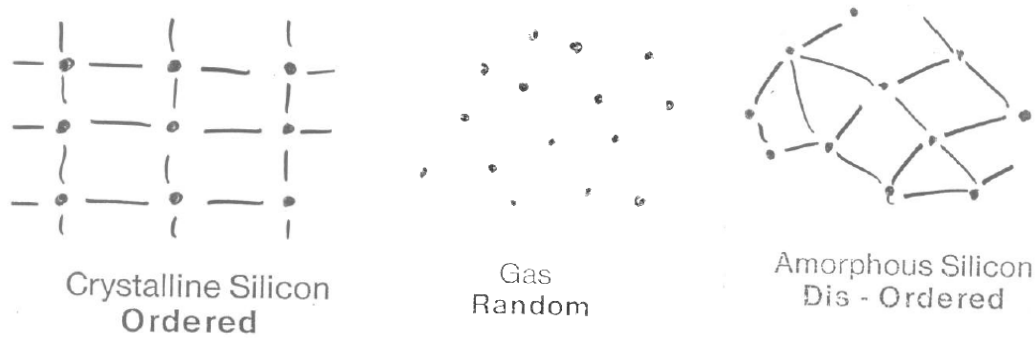
Figure 2. The properties of highly ordered and random materials are able to be described physically, but amorphous silicon being a mixture of the two structures remains poorly understood.

The processing of amorphous silicon is much simpler than crystalline silicon; it can be deposited either by a Physical Vapor Deposition (PVD) method such as sputtering a silicon target or a Chemical Vapor Deposition (CVD) method such as Plasma Enhanced Chemical Vapor Deposition (PECVD) of precursor gases such as silane (SiH_4). The production of crystalline silicon requires temperatures of more than $1200^{\circ}C$ whereas amorphous silicon of high electronic quality (that is, lowest dangling bond defect density and highest electronic drift mobility) can be deposited at temperatures as low as $250^{\circ}C$ which allows it to be grown onto flexible substrates such as plastics.

Amorphous silicon is used as the active semiconductor layer in thin film transistors employed in various consumer electronics devices that do not require extremely fast switching times or very high on/off ratios. Amorphous silicon based thin film transistors (TFT's) are used as a back plane for liquid crystal displays and large area

5

medical x-ray devices, where the a-Si:H records the charge density induced by exposure to x-rays. Using a-Si:H detectors rather than photographic film reduces the patient's exposure dose of x-rays and shortens the required exposure time.[7] As these devices can be made over large areas, a patient's entire chest or upper body can be digitally imaged with fewer exposures and the resulting digital image can be easily transferred and stored.

Amorphous silicon can also be doped n- or p-type, enabling the construction of p-n and p-i-n junctions, where the i- is the intrinsic, or undoped region. The absorption depth of visible light in a-Si:H is on the order of a micron. Hydrogenated amorphous silicon films are typically synthesized in a Plasma Enhanced Chemical Vapor Deposition system, in which films of the order of one micron or thinner can be easily deposited over large areas (1 square foot or larger). The ability to construct a-Si:H based p-i-n devices of this thickness, rather than the millimeter thickness of single crystalline silicon wafers, results in less material being needed, waste material is reduced, and the processing time of the solar cell is decreased.

1.b.- Film Growth

The hydrogenated amorphous silicon films studied in this thesis were synthesized in a Plasma Enhanced Chemical Vapor Deposition (PECVD) reactor, the technique most commonly used in industrial applications of a-Si:H. Silane gas flows through a reactor, and RF power is applied to the capacitively coupled electrodes. The silane molecules are

6

unstable against disassociation when an electronic level is excited roughly 12 eV above the ground state, and the RF power thus generates various charged and neutral radical species, such as SiH_3, SiH_2, Si, H, H_2 among others.[8] The dominant growth mechanism for a-Si:H involves the adhesion of SiH_3 radicals to the growing film surface. Collisions with other radicals break Si-H bonds, enabling additional radicals to chemically bond to the film surface. The resulting films typically contain 10 atomic percent hydrogen, and is considered an alloy of silicon and hydrogen.[9] Deposition at elevated temperatures, typically from 250°C to 300°C provide sufficient surface diffusion to minimize strain in the growing silicon network. Growth at lower temperatures yields more defective material when surface diffusion is inhibited, while at higher temperatures hydrogen evolves from the film during synthesis. Superior opto-electronic properties are typically found in materials deposited at relatively low RF power densities, on the order of 3 W/100 cm^2), which yields film growth rates of roughly 1 – 3 Å/sec.

1.c.- The Staebler-Wronski Effect

The ability to inexpensively deposit a-Si:H over large areas, combined with its large photosensitivity in the visible portion of the solar spectrum, makes this material attractive as the absorption layer in photovoltaic devices. However, its potential as a high efficiency renewable energy source is limited due to the creation of light-induced defects, commonly referred to as the Staebler-Wronski Effect (SWE).[10]

The instantaneous photoconductivity induced in a-Si:H when illuminated with 200 mW/cm^2 of heat-filtered white light from a W-Ha lamp (approximating the intensity and spectrum of solar illumination) can be up to five or six orders of magnitude larger than the dark conductivity. However, this photoconductivity is observed to decay with extended light exposure for exposure times of several hours or longer. Moreover, when the illumination is stopped, the conductivity does not return to its original value, but can be significantly lower, as illustrated in Figure 3. For some a-Si:H films this post-illumination degradation of the dark conductivity can be up to four orders of magnitude.[10] This post-illumination condition is referred to as State B, in contrast to the pre-illuminated, annealed State A. While this effect was first observed in a-Si:H thin films, the efficiency of a-Si:H based solar cells is found to similarly decrease with extended exposure. These photo-induced changes in the electronic properties are reversed upon annealing the material in the dark at 150°C. This light-induced metastable conductance change was first described by David Staebler and Chris Wronski, after whom it is named.

Photoconductivity vs. time
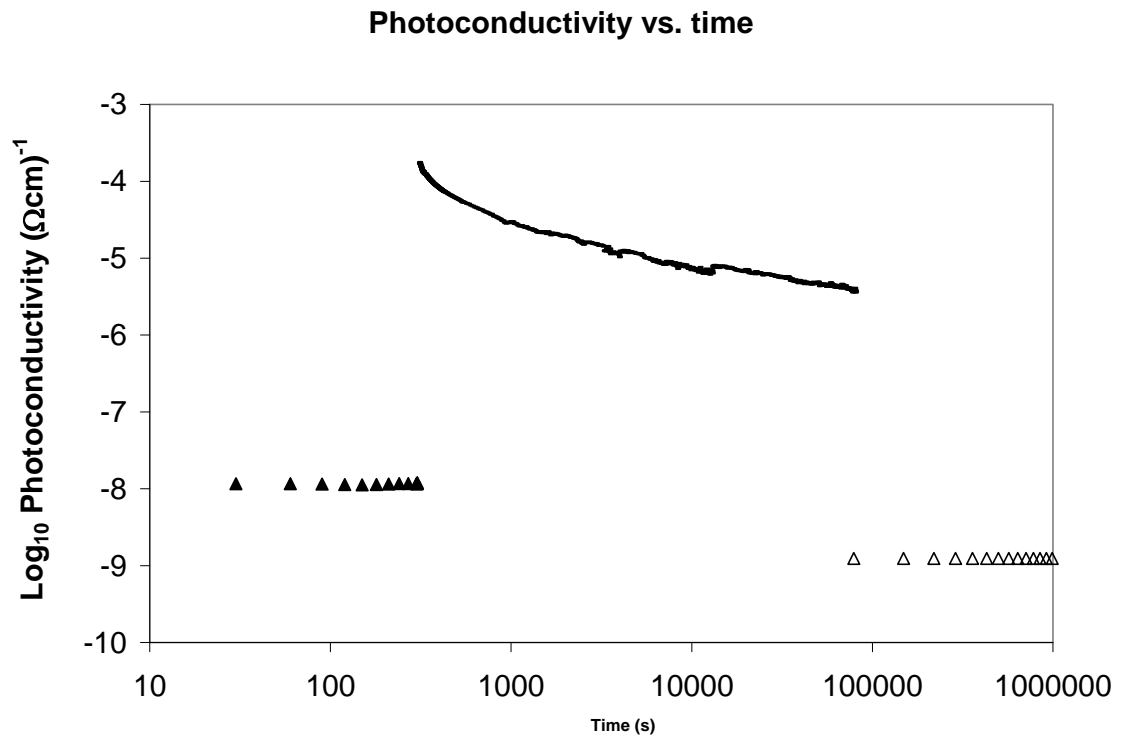
Figure 3. Plot of the conductivity against time for a-Si:H before, during, and following extended illumination with heat-filtered white light. The dark conductivities are denoted by the triangles, with the filled triangles being the State A dark conductivity and the open triangles being the State B dark conductivity, while the photoconductivity is denoted by the line.

Experimental investigations have determined that it is not the absorption of light directly, but rather the recombination of photo-excited electron-hole pairs that leads to the metastable conductance changes. Despite over thirty years of study, there is still considerable uncertainty regarding the microscopic mechanism underlying the SWE. There is a consensus that the SWE is accompanied by an increase in dangling bond

defects that are removed upon annealing, and that the motion of bonded hydrogen is involved in the defect formation/stabilization process. One proposed mechanism involves the breaking of strained silicon bonds that result in the generation of dangling bonds that serve as recombination centers for charge carriers, thereby reducing the photoconductivity. These excess midgap defects shift the Fermi energy away from the conduction band edge due to a statistical shift, decreasing the dark conductivity. These dangling bond defects are suggested to be stabilized by the motion of bonded hydrogen, as indicated by the sketch in Figure 4. Other models also involve the trapping of charges, or the breaking of Si-H bonds.[11-12]

The bonded hydrogen in a-Si:H passivates defects and relieves strain in the material, consequently one cannot simply remove the hydrogen to eliminate the SWE, for the resulting unhydrogenated material has orders of magnitude more dangling bonds than a-Si:H even following light-soaking, and would be useless from a technological standpoint. Most approaches to eliminating the SWE have focused on modifying the material's properties, such as lowering the bonded hydrogen content, without degrading the opto-electronic properties that make the material technologically useful in the first place. Studies of a-Si:H synthesized by alternative techniques suggest that films with a lower bonded hydrogen content can exhibit improved resistance to the SWE. In particular, a-Si:H deposited via a Hot-Wire technique have much lower hydrogen concentrations (approximately 1 at. %, compared to 8 – 10 at. % in PECVD films) and display a smaller metastable conductance change following extended illumination.[13-16]

10

Nuclear Magnetic Resonance studies indicate that the hydrogen in Hot-Wire deposited a-Si:H primarily resides in clusters, such as the inner surface of divacancies, and that the bulk of the amorphous matrix is depleted of bonded hydrogen, yet does not have an excessively high dangling bond density. There is considerable interest in finding techniques to reproduce these conditions in PECVD films, which are more compatible with industrial large-scale, high throughput deposition requirements.
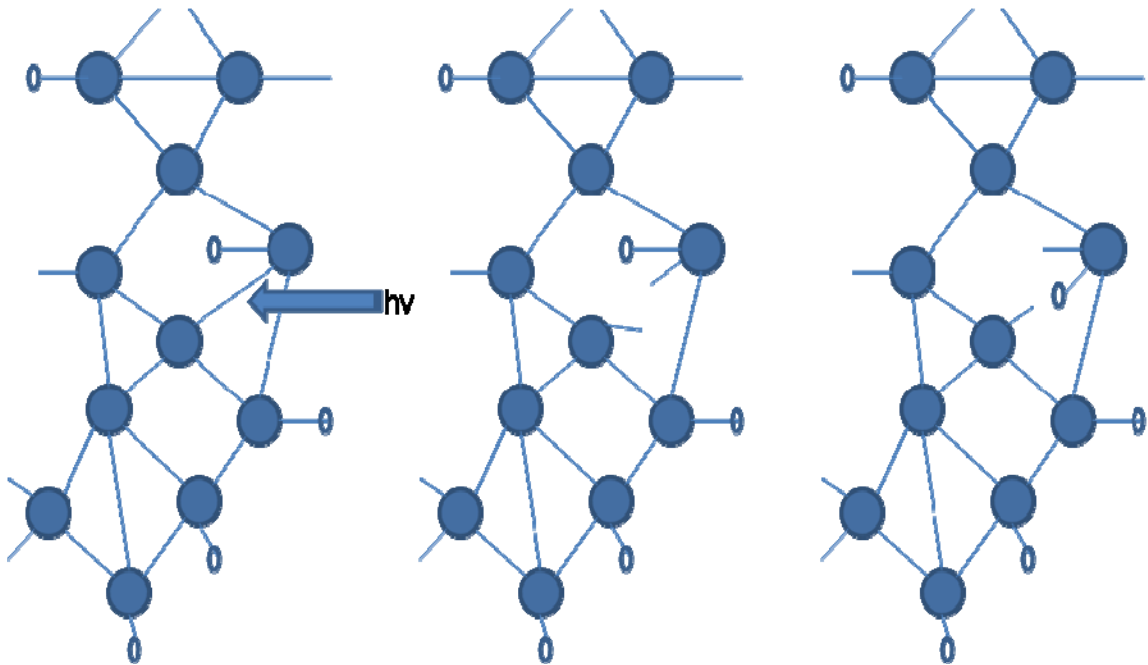
Figure 4. Passivation of dangling bonds through the use of hydrogen dilution. The hydrogen breaks weak bonds reducing strain and also terminates dangling bonds.

One promising approach that has recently attracted considerable attention involves the synthesis of a mixed phase a-Si:H film in which silicon nanocrystallites are embedded in the a-Si:H matrix.[17-20] Mixed phase thin films have recently attracted considerable attention for a variety of applications.[21-23] Silicon nanocrystals embedded in

11

a silicon oxide matrix have been developed as non-volatile memory elements, and for efficient electron emitters, while silicon nanoparticles in a silicon nitride matrix have been fabricated for electroluminescent devices. These materials have been reported to exhibit an improved resistance to the SWE without an increase in the intrinsic dangling bond density, high solar conversion efficiencies coupled with high deposition rates.[24] The modification of the strained-bond distribution of the amorphous network surrounding each silicon nanocrystallite has been suggested to inhibit the light-induced degradation effect in a/nc-Si:H films.[25]

In this thesis, we describe the deposition and characterization of the opto-electronic properties of mixed phase a/nc-Si:H films. As described below, the deposition conditions necessary for particle formation in a single PECVD chamber are very far from those found to be optimize the electronic quality of thin film a-Si:H. This has motivated our investigations of mixed phase a/nc-Si:H films synthesized in a novel dual chamber co-deposition system that is distinct from both polymorphous or protocrystalline deposition.

2.- Materials Preparation

Amorphous silicon is normally produced in a single plasma deposition chamber under low pressure (< 400 mTorr), low RF power, and at and elevated substrate temperatures, typically 250°C. As the applied RF power increases, the deposition rate rises. In this case the SiH$_3$ radicals strike the growing film surface faster than the surface atoms can find a relative equilibrium configuration. Materials deposited at too high an RF power have higher densities of dangling bond defects (which degrade the electronic properties of the film) and greater long-range disorder, as characterized from electronic transport measurements. A decrease in resistance is observed in films deposited at lower gas chamber pressures; however the deposition rate also decreases causing the processing time to increase. The substrate temperature during film growth also plays an important role in determining the electronic quality of the a-Si:H film.[26-27] At low temperatures the deposition radicals from the plasma do not have enough thermal energy for surface diffusion to enable the silicon and hydrogen atoms to achieve their equilibrium positions. Consequently films deposited at low substrate temperatures have high defect densities and high concentration of strained silicon-silicon bonds. Conversely in films deposited at too high substrate temperatures the surface radicals have sufficient energy for hydrogen to evolve from the growing material, leaving dangling bonds without passivation. These films similarly have a high defect density and poor transport properties. The optimal film quality is achieved in films deposited at low RF power levels of about 1 − 3 W for

13

electrode areas of 100 – 200 cm^2, and substrate temperatures of approximately 250 – 300°C.

Many groups have adopted differing approaches to depositing silicon nanocrystals within a hydrogenated amorphous silicon matrix. Many mixed phased films are produced under growth conditions conducive to powder formation in the plasma. Depending on the detailed conditions under which these mixed phase materials are synthesized, these materials are termed polymorphous silicon (pm-Si:H), protocrystalline silicon (pr-Si:H) or, amorphous silicon with nanocrystalline inclusions (a/nc-Si:H, the nomenclature that we prefer and that will be employed in this thesis).[28-29]

Polymorphous silicon is deposited under high gas chamber pressures, such that particulates form within the plasma that can then diffuse to the growing film surface and be incorporated into the amorphous silicon matrix.[30] In order to regulate the silicon nanocrystallite diameter, the silane gas is heavily diluted with hydrogen, which etches the particulates formed in the plasma and maintains the nanoparticle size.[31-32] Polymorphous silicon has a structure between amorphous silicon and microcrystalline silicon, being an amorphous material with nanoparticles embedded into the film.[30, 33] The precursor gases for these films have been diluted not only using Hydrogen but also using Helium. These films have been reported to display improved photoconductivity compared to conventional a-Si:H films.[34] These films are produced near the edge of powder formation and can be thought of more as a process involving powder management. Powders are

14

created in the silane plasma when both the RF power is high along with the deposition pressure. The agglomerates that form these powders are microns in size and would be detrimental during normal processing of devices that have thicknesses on the order of microns themselves. These powders can be controlled using thermal gradients, silane gas flow rates, and hydrogen dilution.

Protocrystalline films, on the other hand, are deposited near conditions that induce crystallite formation in the silicon film itself. To produce polymorphous, protocrystalline, and microcrystalline silicon films all require high gas pressures and high rf power, but the extent of the pressure determines the type of film. At moderately high pressures the film produced will be microcrystalline while at extremely high pressures polymorphous films will be produced. Protocrystalline films are created in the range between the two, where a polymorphous film does not grow, but a microcrystalline film will start to form if a sufficiently thick film were deposited. Greater thicknesses can be achieved by increasing the total gas pressure to making the growth conditions closer to the polymorphous film or by decreasing the temperature at which the substrate is held, thereby delaying the onset of crystallization.[31] Polycrystalline silicon is used in the fabrication of metal-oxide semiconductors and thin film transistors. When these films contain small crystallite grains, they have high defect densities at grain boundaries. Hydrogen has been used to reduce these defect concentrations, but the hydrogen dilution also increases the resistivity of these films.[35] Both protocrystalline and polymorphous silicon have been observed to display both an improved resistance to the Staebler-Wronski Effect and high quality

15

transport properties.[36]   One particular difference between the two materials is that the crystalline fraction of the protocrystalline films changes with the film's thickness whereas polymorphous films retain a constant crystalline fraction throughout the bulk material. These films and their growth mechanisms have been evaluated to develop the optimum parameters to deposit microcrystalline silicon.

2.a - Mixed Phase Materials - Single Chamber Deposition

Hydrogenated amorphous silicon thin films containing silicon nanocrystals (a/nc-Si:H) can be synthesized in a capacitively coupled Plasma Enhanced Chemical Vapor Deposition (PECVD) system, under plasma conditions (heavy hydrogen dilution of silane and chamber pressures significantly above 500 mTorr) near the edge of powder formation, where the powder consists of particles that may be several tens of nanometers in size within the plasma. The hydrogen dilution of the silane inhibits the growth of larger particles, and under certain conditions smaller silicon clusters and crystallites, with diameters as small as 1 nm, are formed in the plasma and incorporated into the growing film. Silicon nanoparticles have also been synthesized in an Inductively Coupled Plasma system, where the average nanoparticle diameter is controlled by the gas pressure and plasma on time (that is, the time for which the plasma is pulsed on).[37]

The single chamber PECVD system, sketched in Figure 5, employs 5% silane diluted in helium that can be further diluted with hydrogen. When the silane is not heavily diluted with hydrogen gas, the resulting nanoparticles are amorphous rather than crystalline, raising the possibility of investigating the electronic properties of hydrogenated amorphous silicon (a-Si:H) nanoparticles.[38] The films deposited with hydrogen dilution of the silane used a hydrogen dilution ratio, $R = [H_2]/[SiH_4]$, of 50 when producing a mixed phased film and a hydrogen dilution ratio of 0 when producing purely amorphous films. In this system the deposition gases enter the chamber through the top showerhead RF electrode. Substrates rest on the lower, grounded electrode (each electrode has an area of approximately 200 cm^2). The a/nc-Si:H films were deposited with R = 50, at a pressure of ~ 360 – 1800 mTorr and an RF power of 15-20 W, and were roughly 0.1 μm thick. Films grown with heavy hydrogen dilution exhibit a greater tendency to peel off the glass substrates when the film thickness exceeds 0.5 μm. The substrates were cleaned with a hydrogen plasma for about five minutes at a pressure of ~ 260 mTorr and an RF power of 20 W prior to deposition.
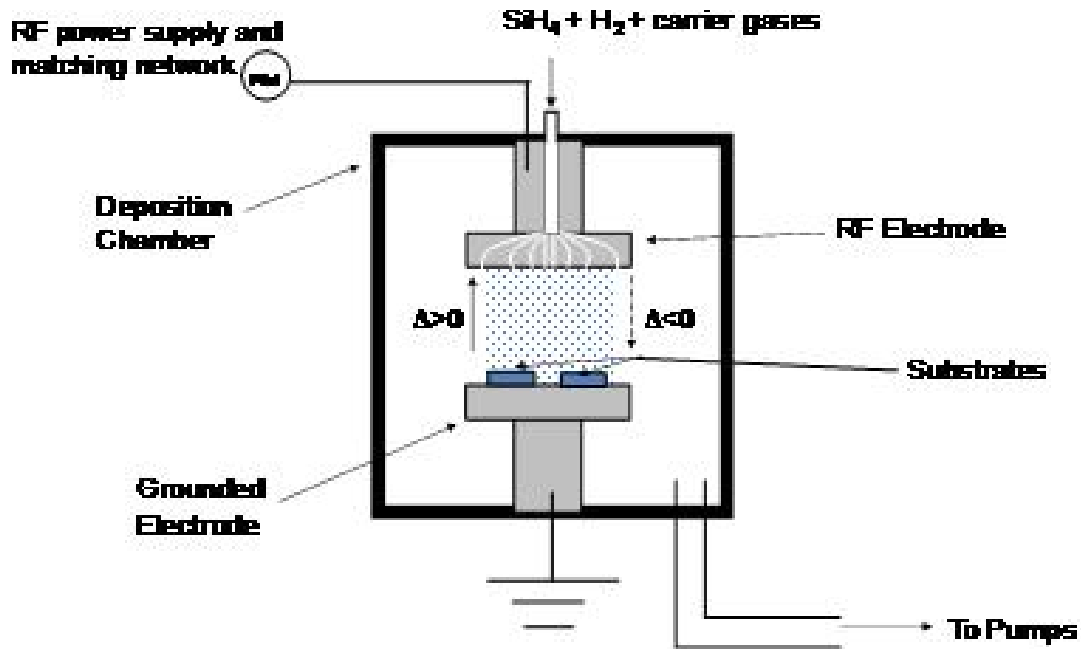
Figure 5. Sketch of the single chamber deposition system used to grow a/nc-Si:H films. The mixed phase thin films are deposited onto substrates on the heated, grounded electrode for further study.

In order to vary the concentration of nanocrystallites that are embedded within the a-Si:H matrix, one must be able to direct the nanoparticles either toward or away from the growing film surface. Particles in a plasma rapidly acquire a negative charge (owing to the higher energy and mobility of electrons compared to positively charged ions within the plasma) and are therefore repelled from the negatively charged sheath regions. These trapped charged particles can be moved either toward or away from the growing a-Si:H film surface by either convective drag forces or thermophoresis forces.[39] The latter arise when a thermal gradient is applied across the two capacitively-coupled plates in the

18

PECVD system. In the conventional configuration for depositing a-Si:H in a PECVD system, only the grounded electrode is intentionally heated, which is defined as a positive thermal gradient that drives particles away from the film's surface. The RF electrode can be heated to the same temperature as the grounded electrode producing a zero thermal gradient that allows particles to deposit onto the film's surface. In addition, the RF electrode can be heated to a temperature greater than the grounded electrode creating a negative thermal gradient that drives particles into the film.

Both of the electrodes in the system in Figure 5 may be independently heated, allowing the thermal gradient between the electrodes to be controlled during deposition.[40] The grounded electrode is heated by a resistive heater coil (this approach to heating an electrode is commonly employed in PECVD systems), while the RF electrode cannot be heated electrically. A quartz lamp heater (Kurt J. Lesker QLH0500) was consequently mounted in the reactor chamber, above the RF electrode. This single lamp assembly employs a 500 W bulb and can heat the RF electrode to approximately 525 K. The thermal gradient is here defined as the difference between the temperature of the grounded (deposition) electrode (T_G) and the temperature of the RF electrode (T_{RF}), divided by the electrode separation (d):

$$\Delta T \equiv \frac{T_G - T_{RF}}{d}$$

The separation between electrodes is kept fixed at $d = 4$ cm. The thermal gradient is illustrated in Figure 5, where the direction of the gradient (from hot to cold) is indicated by the labeled arrows for the cases of $\Delta T > 0$ and $\Delta T < 0$. The traditional configuration for amorphous silicon deposition, with the grounded (deposition) electrode heated and the RF electrode unheated would correspond to a positive thermal gradient by the definition above.

An elevated temperature of 523 K is desired for the deposition electrode during the growth of the a-nc/Si:H films.[41] A positive gradient of +56 K/cm corresponds to the deposition electrode temperature of 523 K and the RF electrode unheated (~ 300 K). A thermal gradient of zero corresponds to both electrodes having a temperature of 523 K. As this was the highest temperature to which the RF electrode could be raised, the negative thermal gradient of -25 K/cm was achieved with the deposition electrode temperature of 423 K and the RF electrode temperature of 523 K. Previous studies of the influence of the deposition temperature on the a-Si:H film's opto-electronic properties find only a minimal effect on electronic quality for substrate temperatures of 423 K, compared to films grown at 523 K.[42]

2.b - Mixed Phase Materials - Dual Chamber Deposition

While mixed phase materials can be synthesized in a PECVD system operated at high silane gas chamber pressures, where silicon cluster formation is known to occur, the

20

plasma conditions that yield silicon nanocrystals are far from those that are known to produce high electronic quality a-Si:H. In addition, the concentration of silicon particles embedded within the a-Si:H matrix is not easily controlled, even with the thermophoresis effect. We have consequently constructed a dual chamber co-deposition system, where the silicon nanocrystals are formed in one plasma deposition system, and are then entrained in a carrier gas and injected into a second PECVD system, where hydrogenated amorphous silicon is deposited.[43] A benefit of the dual chamber co-deposition system is that one is not limited to growing silicon nanocrystalline particles in an a-Si:H film. In order to optimize the properties of mixed phase materials, it would be advantageous to have independent control over the structure of the a/nc-Si:H film in terms of crystallite size and number density. A sketch of the dual chamber co-deposition system is shown in Figure 6.
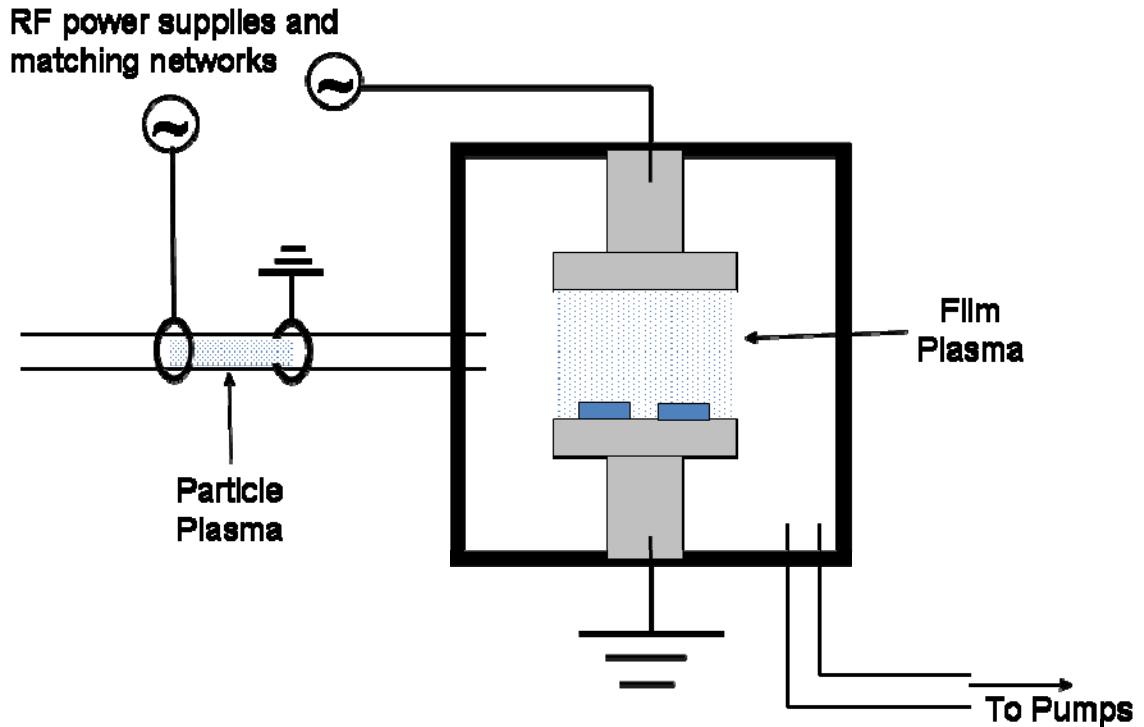
Figure 6. Sketch of the dual chamber co-deposition system. Nanocrystallites are synthesized in a plasma upstream at high gas pressure and high rf power. The particles are then injected into the second chamber where the nanocrystallites are incorporated into a film being deposited by a second plasma where the rf power and gas pressure are lower.

Crystalline nanoparticles 3-5 nm in diameter are produced in an upstream flow-through reactor and, entrained in an inert carrier gas, then introduced into the second amorphous silicon deposition reactor. As described in section 2a, these particles are negatively charged (owing to the higher energy and mobility of electrons compared to positively charged ions within the plasma) and are therefore repelled from the negatively

charged sheath regions. These trapped charged particles can be moved either toward or away from the growing a-Si:H film surface by either convective drag forces or thermophoresis forces.[39, 44] We have employed both techniques to control the nanocrystallite density in a/nc-Si:H in the dual chamber co-deposition system. However, we have discovered that it is difficult to produce mixed phase films with a high crystalline volume fraction using thermophoresis to control nanocrystallite incorporation into the amorphous film.

A more annotated sketch of the dual chamber deposition system is shown in Figure 7. A 13.56 MHz RF plasma is excited in a 3/8 inch diameter quartz tube with two fitted ring electrodes from a mixture of 5% silane diluted in helium (flow rate 10 sccm).[45] The plasma conditions in this particle synthesis reactor (pressure of 1.5 Torr, RF power of 10 W) are selected for the formation of silicon nanocrystals of diameter 3-5 nm. Previous studies have confirmed that the particles generated in the particle synthesis reactor are indeed crystalline, with a nearly monodisperse size distribution set by the detailed plasma conditions.[46] The tube is attached to the side of a grounded second Capacitively-Coupled Plasma (CCP) chamber. The plasma in the particle synthesis reactor is extinguished at the point of connection, and a flow of an inert carrier gas of argon (flow rate 50 sccm) is used to entrain the particles into the second chamber. A mixture of 5% silane diluted in helium is introduced into this chamber via the top showerhead electrode. A 13.56 MHz RF plasma is excited in the second chamber at a total pressure of 430 mTorr with RF power of 3 W, leading to the deposition of a-Si:H.

23

Substrates placed on the lower grounded electrode are used for the structural and electronic characterization measurements described here.

The nanocrystalline particles are injected at the midpoint between the RF and grounded electrodes in the second CCP chamber, as shown in Figure 7, and are sensitive to a thermophoresis force. Traditionally the lower, grounded electrode is heated to 250°C (as previous research has indicated that films grown at this substrate temperature have superior charge transport properties compared to lower or higher deposition temperatures) and the top RF electrode is unheated. Consequently there is a positive thermal gradient creating a thermophoresis force directed away from the lower deposition electrode, which tends to push any particles away from the growing film surface. Assuming that the top electrode remains at room temperature during plasma deposition, for a 5 cm plate separation the thermal gradient is taken to be approximately $\Delta T = +50$ K/cm. As described in section 2a, the top RF electrode may be also independently heated during a plasma deposition run, and have also grown a/nc-Si:H films under identical conditions as for when $\Delta T = +50$ K/cm, except that the top electrode is also at 250 C ($\Delta T = 0$) or when the substrate temperature is 220 C, the top electrode is heated to 320 C ($\Delta T = -20$ K/cm). These latter two conditions would either allow particle motion to the growing a-Si:H surface via Brownian diffusion when $\Delta T = 0$, or actively push particles toward the film when $\Delta T < 0$. Note that the thermal gradients across the plasma in the dual chamber co-deposition system have different values than in the single chamber system described in section 2a.
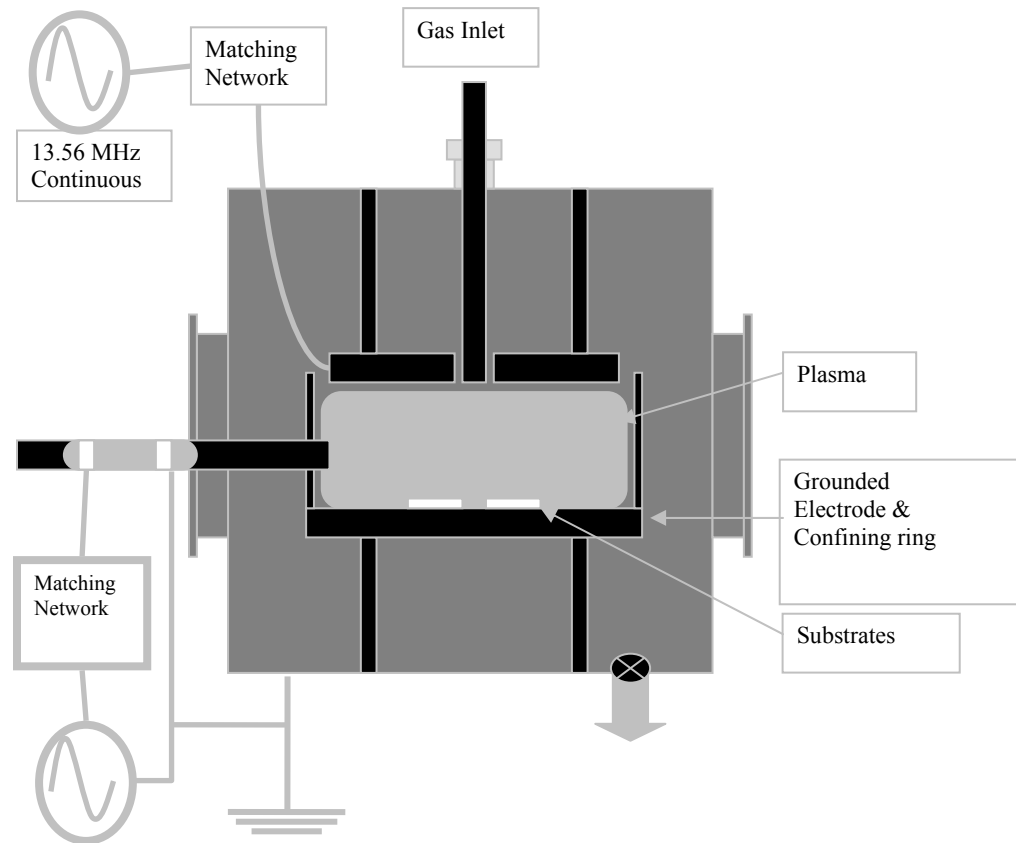
Figure 7. More detailed sketch of the dual chamber co-deposition system. Nanoparticles are synthesized in the first chamber, shown to the left, at high pressure and RF power. These particles are then injected into the second capacitively-coupled chamber where hydrogenated amorphous silicon is deposited at a lower gas pressure and RF power.

2.c - Doped Mixed Phase Materials - Dual Chamber Deposition

Neither the single chamber PECVD system in Figure 4 or the dual chamber co-deposition system in the Low Temperature Plasma Laboratory at the University of

Minnesota (Figure 6) are configured to grow doped a-Si:H films. In fact, in order to avoid issues involving unintentional contamination, dopants have deliberately never been introduced into these systems. We have consequently constructed a separate dual chamber co-deposition system that enables the synthesis of doped mixed phase materials, using either phosphine or diborane as dopants. The polymorphous and protocrystalline films investigated by other labs have been on undoped materials. Mixed phased films with dopants have not been previously investigated and would be interesting to study for application in devices that require p- and n-type layers.

This system employed to synthesize doped mixed phase films is shown in Figure 8. Reactive gases consisting of silane (SiH_4) and phosphine (PH_3), diluted with a carrier gas of argon, are first passed through the Particle Synthesis Reactor, which consists of a 3/8 inch diameter quartz tube with two fitted ring electrodes, connected to a 13.56 MHz power supply and matching network. Silane and phosphine are dynamically mixed, and diluted with an inert carrier gas of argon; a total gas flow rate of 90 sccm was maintained through both chambers. The plasma conditions in the Particle Synthesis Reactor (1.7 Torr, 70 W RF power) were selected to generate silicon nanocrystals, that were then carried by the flowing argon into the second PECVD chamber (700 mTorr, RF power 4 W). The flow rates were adjusted to control both the nanoparticle and doping concentration. The silane flow rates varied between 2.5 sccm and 5.5 sccm corresponding to high nanocrystalline particle concentration to low nanocrystalline particle concentration, where the conditions governing the nanocrystalline diameter are

26

fixed. The doping concentration was changed by changing the flow rates of dopant gas to produce doping concentrations between $[PH_3]/[SiH_4] = 6 \times 10^{-5}$ and $[PH_3]/[SiH_4] = 6 \times 10^{-2}$. Mixed phase a/nc-Si:H films are deposited on substrates held at 250^0 C placed on the lower, grounded electrode in the second PECVD chamber.
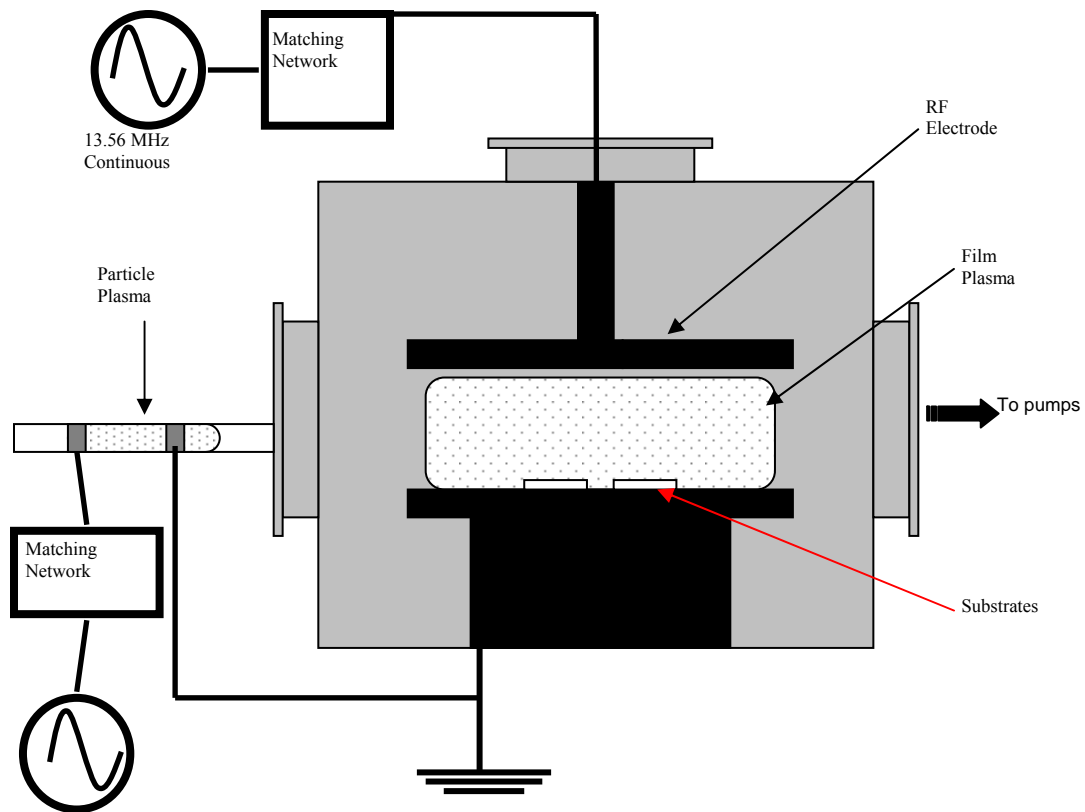
Figure 8: Sketch of the dual chamber co-deposition system used to grow doped a/nc-Si:H films. Dopant gases and silane pass through the particle deposition chamber (left) and then flow into the second chamber where the amorphous silicon film is deposited.

The samples were deposited onto Corning 7059 glass substrates and crystalline silicon substrates for infra-red absorption measurements. Film thicknesses are measured using a profilometer, and deposition rates are determined by dividing the film thickness by the deposition time of 62 minutes. Co-planar chromium electrodes (0.2 cm wide, 1 cm long) for electronic measurements are deposited using a shadow mask via e-beam evaporation.

The precursor gases in the film deposition chamber is the residual gas of the particle chamber so there is also an issue of where the dopants are incorporated in the mixed phase films. It would be possible at the two extremes of doping efficiency of the nanoparticles to have either undoped nanoparticles in a doped film or doped nanoparticles in an undoped film. It has been seen that the doping efficiency of the nanocrystals is near 100% up to ~4% phosphorus doping.[47] Even though it would appear that the dopant gas should be completely consumed in the nanoparticles chamber and the a-Si:H matrix film should be undoped for the doped mixed phase films, it was observed, as described below, that doped mixed phase film's conductivity was indeed enhanced, similar to observations of doped films without nanocrystallite inclusions.

3.- Characterization Methods

Following the successful deposition of mixed phase a/nc-Si:H films, the quality of the film and details of its physical composition were characterized. Structural, electrical, and optical characterization techniques employed included profilometry to verify the film thickness, temperature dependence of the dark conductivity to determine the activation energy of the film, photoconductivity as a function of time to determine the photosensitivity and effects of light-induced defect creation, Fourier transform infrared spectroscopy (FTIR) to determine the concentration and local bonding structure of the hydrogen in the a-Si:H films, constant photocurrent method (CPM) to measure the spectral dependence of the optical absorption coefficient, which provides a measure of the defect states of the film, high-resolution transmission electron microscopy (HRTEM), RAMAN spectroscopy to determine the crystalline fraction (if any) of the mixed phase films, and thermopower measurements.

For both the single chamber and dual chamber co-deposition systems, films were deposited onto Corning 7059 (low sodium content) glass substrates for opto-electronic characterization and onto crystalline silicon wafer substrates for infra-red absorption measurements. Coplanar chromium electrodes were e-beam evaporated onto the films, these electrodes yielded linear current-voltage characteristics. Films investigated with transmission electron microscopy (TEM) were 10 nm thick and deposited onto cleaved NaCl substrates.[48] These films were then removed by dissolving the salt substrates in

distilled water and floating the films onto a 3 mm copper TEM grid.[49] The samples were then allowed to air dry in desiccators prior to TEM study.

3.a.- Profilometry

Profilometry, a process similar to a needle moving along the surface of a record, is used to ascertain the film thickness providing a determination of both the deposition rate and the geometry factor for conductivity measurements. The sample is prepared with a step by masking off a portion of the substrate during deposition so that a sharp edge is created, with an approximately discontinuous step between the substrate and the a-Si:H film. The Dektak profilometer in the Nanofabrication Facility has a diamond stylus that is lowered until it comes into contact with the glass substrate where it slides along the sample with a constant force until it is deflected at the step and continues to slide on the film's surface (see Figure 9). The amount of the deflection directly related to the thickness of the film, is detected using a laser beam focused onto the back of a probe holding the stylus. The mixed phase films studied here are typically 300 to 1000 nanometers thick.

As the inclusion of silicon nanoparticles can change the thickness of the resulting mixed phase film, care must be taken when ascertaining the film thickness, to be used in other characterization measurements. The force of the stylus was kept low to avoid deformation and delamination of the film. The sampling rate was also low as only a few

points are needed to detect the height of the step edge. However, the scan speed was high

at 200 μm/s so that long scans (greater than 3 mm) could be rapidly acquired. Long

scans were desired so that there would be suitable data taken along the glass substrate as

well as along the surface of the film. In addition, the thickness of the film is determined

at three different locations along the film so that an average thickness of the film can be

calculated.
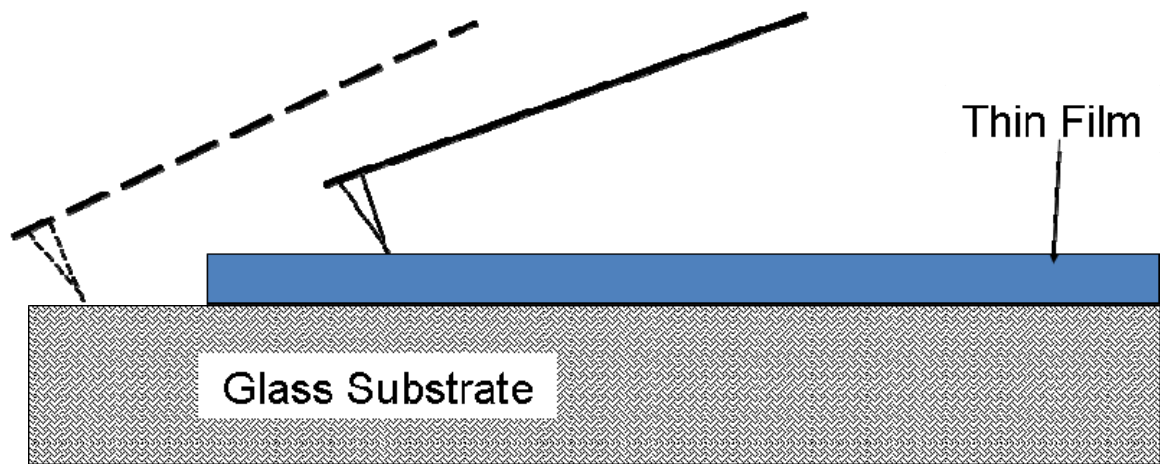
Figure 9. Sketch of the profilometer set-up. The stylus sweeps from the left along the

glass substrate and onto the top of the thin film detecting the film thickness.

3.b.- Dark Conductivity and Photoconductivity

The electrical conductivity is measured using coplanar chromium electrodes that

are deposited onto the surface of the amorphous semiconductor. The electrodes are

typically 1 cm long and separated by a gap of either 2 mm or 4 mm. The samples described here always exhibited linear current-voltage characteristics over the range of applied voltages investigated. A constant DC voltage is applied to one electrode while the current flowing through the film is measured from the second electrode using a Keithley picoammeter or femtoammeter. The sample sits on a copper block inside a vacuum chamber. Resistive heaters can increase the temperature of the block, and the conductance of the semiconductor is measured as a function of temperature over the range of 320K to 450K. The conductivity of the amorphous silicon film is described by the expression

$$\sigma = \sigma_0 \exp(-E_a/k_B T)$$

where σ_0 is the conductivity prefactor, E_a is the activation energy of the film, k_B is Boltzmann's constant, and T is the Absolute temperature. The Arhennius plot provides a measure of the conductivity and the activation energy of the film in its annealed state (State A), and after light soaking (State B).

When measuring the conductivity, the sample is first annealed at 450K in the dark for 120 minutes to remove any light induced defects from the Staebler-Wronski effect and any surface adsorbates such as water vapor.[50] The sample is then cooled slowly at a rate of 1 K/minute to 320K where the film is then in State A. The film is then heated again to 450K with the current recorded at 3 degree intervals. The film is then allowed to

cool ambiently to room temperature. In order to investigate the magnitude of the Staebler-Wronski effect in these films, a light soak is then performed.[10, 51] The film is illuminated with heat-filtered white light from a W-Ha lamp (intensity approximately 100 mW/cm^2) for a given light exposure, typically 22 hours. Following this illumination, the dark conductivity in the light soaked State B as a function of temperature is then remeasured upon warming.

The relationship between the initial photoconductivity and the State A dark conductivity is defined as the photosensitivity. The photosensitivity is written as

$$\sigma_{sensitivity} = \sigma_{photo}/\sigma_{dark}$$

The photoconductivity, σ_{photo}, is determined by the product of the photo-excited charge carrier generation rate G and the recombination lifetime τ_{rec} and the electron charge and mobility, that is $\sigma_{photo} = G \tau_{rec} e \mu$. The recombination lifetime can be expressed as $\tau_{rec} = 1 / (N_{rec} v s)$ where N_{rec} is the density of localized states that act as recombination centers, v is the charge carrier's thermal velocity and s is the capture cross-section of a particular recombination center (we use s for the capture cross-section to avoid confusion with the conductivity σ). The degradation of the photoconductivity during extended illumination in the Staebler-Wronski effect is ascribed to the creation of metastable dangling bond defects in the middle of the mobility gap, which act as

additional recombination centers, decreasing τ_{rec}. One should note that one method by which a film could display a reduced SWE is if it has a very high defect density in its annealed, State A. In this case, if the dangling bond density in State A is about 10^{18} cm^{-3}, then the addition of another 10^{17} cm^{-3} defects in the SWE will have a negligible effect. The motivation of the mixed phase project is to produce materials of high electronic quality, one measure of which is a low dangling bond density in Sate A, that also resist the introduction of additional light induced defects.

3.c.- Fourier Transform Infra-Red Spectroscopy

Fourier transform infra-red (FTIR) spectroscopy is employed to characterize the relative hydrogen composition of the films. The intensity of infrared light transmitted through the sample is recorded as a function of frequency (though one typically discusses the infra-red spectrum in terms of the light's wavenumber). Light of sufficient energy to excite a molecular vibrational mode will be absorbed, and in this way differing Si-H and Si-H$_2$ bonds in the thin film amorphous semiconductor can be identified. The same bond may have several distinct vibrational modes, corresponding to stretching, rocking or wagging states. These modes are detected with an interferometer used to measure the absorption of the infrared beam at different wavenumbers.

Si-Si vibrational modes are not infra-red active due to symmetry considerations, while Si-H bonds are easy to detect as they are infra-red active, and in PECVD the

concentration of bonded hydrogen is on the order of ten atomic percent.[52-53] The Si-H

stretching mode is observed at a wavenumber of 2000 cm^{-1}, while a silicon atom bonded

directly to two hydrogen atoms, Si-H$_2$ (the other bonds are taken to be to silicon atoms in

the amorphous network) has been identified with absorption at 2090 cm^{-1}. The

concentration of Si-H$_2$ molecular units, can be characterized through the "microstructure

fraction" R, defined as

$$R = I_{2090}/(I_{2090}+I_{2000})$$

where I_{2000} is the area under the peak at 2000 cm^{-1} and I_{2090} is the area under the peak at

2090 cm^{-1}, found using Gaussian peaks to fit the spectrum. The latter peak has been

associated with higher amounts of structural and electronic disorder,[42, 54-55] and in a/nc-

Si:H films the I_{2090} peak has been identified with the bonded hydrogen in grain boundary

regions surrounding the nanocrystalline inclusions.[56]

Samples for FTIR are deposited on single-sided polished crystalline silicon wafers

(a-Si:H deposited onto the polished face) in the plasma chamber alongside samples

deposited on glass substrates for other measurements. Crystalline silicon is used because

it is transparent to the infrared beam, polished side up so that there is a smooth surface to

deposit on, and single-sided polished as opposed to double-sided polished to reduce

interference fringes in the spectra. Absorption data were acquired using a Nicolet Magna

750 FTIR spectrometer in the Characterizations Facility at the University of Minnesota,

where the transmission through a blank crystalline silicon substrate is used for reference. The measurements were taken with the samples residing in a dry nitrogen atmosphere to reduce the absorption signal from water vapor.

3.d.- Optical Absorption Coefficient - Constant Photocurrent Method

In a-Si:H, the highest occupied band of states arises from the overlap of bonding orbitals between Si-Si atoms, while the lowest unoccupied band results from anti-bonding orbitals. As shown in the cartoon sketch in Figure 10, the density of states in amorphous semiconductors varies continuously with energy. From a high value in the valence band of over 10^{22} cm^{-3} eV^{-1} the density of filled states decreases exponentially with energy, forming a "band tail." Near the edge of the lowest unoccupied band there are equivalent states that also tail off exponentially with energy toward the filled band. While there is not a gap in the density of states between filled and empty bands, as in crystalline silicon, there is a "mobility gap" separating extended states from localized levels. A charge carrier in states at the higher densities of 10^{22} cm^{-3} eV^{-1} would have a mobility of approximately 10 cm^2/V-sec, while states in the band tails would exhibit a much lower mobility.

The density of states at and beneath the conduction band mobility edge and above the valence band mobility edge, play a crucial role in determining the performance of a-Si:H based photovoltaic devices. Measurement of the optical absorption spectra is

therefore an important characterization tool for thin film amorphous semiconductors. As these films typically have a thickness d of one micron or less, conventional transmission spectroscopy techniques are not able to determine absorption coefficient α values less than $\alpha \sim 10^3$ cm^{-1}, corresponding to $\alpha d \sim 1 - 0.1$, where d is the film thickness. One therefore employs either bolometric techniques (sensitive to the temperature rise associated with the absorption of photons) or conductance methods, where the charge carriers excited by the light are electrically detected. Our lab has a system to measure the constant photocurrent method (CPM) of thin film a-Si:H, providing determinations of the absorption coefficient for αd values down to 10^{-4}.[57-59]

The photoconductivity can be written as

$$\sigma_{ph} = n_{ph}e\mu = G\tau\eta e\mu$$

where G is the generation rate, τ the lifetime of the electron, and η the efficiency of the process that is assumed to be ~1. The generation rate can be written as $I_o(1 - e^{-\alpha d})$, where I_o is the incident light intensity. The photoconductivity can then be rewritten as

$$\sigma_{ph} = \tau\eta e\mu \, I_o(1 - e^{-\alpha d}).$$

For $\alpha d \ll 1$, which is the regime in which photoconductivity is most useful, the equation simplifies to

$$\sigma_{ph} = I_o\tau\eta e\mu\,(\alpha d) = (I_o\tau\eta e\mu d)\,\alpha$$

where electron lifetimes, process efficiency, mobility are assumed to remain relatively constant across the spectrum sampled during the constant photoconductivity measurement. The constants independent of wavelength can be grouped together and the absorption coefficient as a function of energy can be explicitly written as

$$\alpha(h\nu) = \sigma_{ph}\,/\,(\tau\eta e\mu d) * 1/I(h\nu)$$

or using a relative scale, the equation can be simplified to

$$\alpha'(h\nu) = constant/I(h\nu).$$

The values obtained can be converted to an absolute scale by performing a one point conversion in a region that the absorption coefficient can be calculated from the transmission of light through the sample.

$$\alpha(h\nu) = \kappa \, \alpha'(h\nu)$$

$$\alpha(h\nu) = (1/d) \ln (I_{glass} / I_{film})$$

where I_{glass} is the intensity of transmitted light at a given wavelength through a glass substrate and I_{film} is the intensity of transmitted light at the same wavelength bulb power setting measured through a silicon film deposited on a glass substrate, α' is the relative absorption coefficient at a particular wavelength, κ is the constant to convert to absolute values, and α is the absorption coefficient in units of cm^{-1}.

Light at specific wavelengths can be used to probe the defect states of the film. The more states available to absorb a given photon, the larger will be the resulting photocurrent. However, strongly absorbed light will cause a shift in the quasi-Fermi levels (to reflect the higher density of photo-excited charge carriers) and this in turn may change the occupancy of localized states in the mobility gap. The ability of these localized states to function as recombination centers may be sensitive to their charge state. Consequently both the density of photo-excited charge carriers and the recombination lifetime will, in general, depend on the magnitude of the optical absorption for a particular wavelength of light. By varying the incident light intensity so that the magnitude of the photocurrent is unchanged at different photon energies, one can ensure that the quasi-Fermi energy, and hence the density of localized state recombination centers, is the same for all photon energies. By noting how much the incident light

intensity had to be adjusted in order to maintain a constant photocurrent, the spectrally resolved optical absorption coefficient can be measured.[57] The above procedure yields relative changes in the absorption as a function of wavelength. By measuring α at one point where using a conventional transmission technique, one can convert the relative absorption values to an absolute scale.

As indicated in Figure 11, there are three ranges that are probed during CPM: valence band to conduction band (region A), valence band to conduction band tail or valence band tail to conduction band (region B), and defect state to conduction band or valence band to defect state (region C). The photon energies corresponding to region A indicate the magnitude of the optical gap for the material. One method to characterize the optical gap in an amorphous semiconductor with a continuous distribution of sates in the mobility gap is through the Tauc gap, defined as:

$$(\alpha E)^{1/2} = B(E - E_G)$$

with E_G being the Tauc (optical) gap, while B is a constant.[60-62] This definition assumes a constant dipole matrix element.

The optical absorption coefficient in region B displays an exponential variation with photon energy, and thus provides a quantitative determination of the exponential

band tail states (see Figure 11).[63]   The photon energy dependence of the optical absorption coefficient in region B can be described by the function:

$$\alpha = \alpha_0 e^{-h\nu / E_0}$$

with E_0 being the Urbach slope. Using Fermi's Golden Rule for the optical absorption coefficient, the Urbach slope E_0 results from a convolution of the roughly parabolic energy dependence of the density of states at and above the mobility edge and the exponential energy dependence of the band tail states. Consequently the Urbach slope is characteristic of the broad band tails, and the larger E_0 the broader the band tails, reflecting increased disorder in the film. High electronic quality a-Si:H has an Urbach slope of 40 – 50 meV.

Dangling bond defects residing in the middle of the mobility gap give rise to sub-bandgap optical absorption (region C) and the magnitude of α at photon energies less than 1.5 eV provides a measure of the defect density.
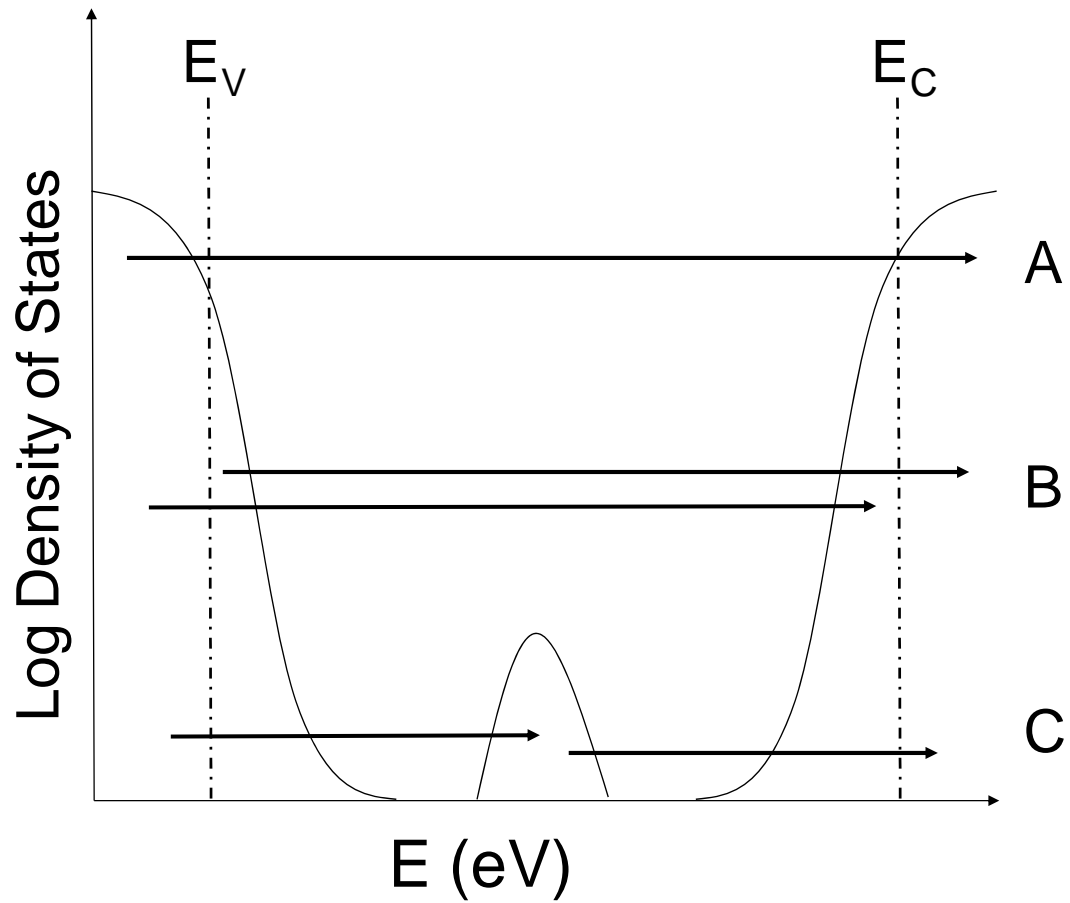
Figure 10.   Sketch of the density of states of a-Si:H as a function of energy.   Band to band transitions are denoted by (A), band tail/band transitions by (B), and defect/band transitions denoted by (C).   These transitions correspond to the three regions in the following absorption coefficient plot.
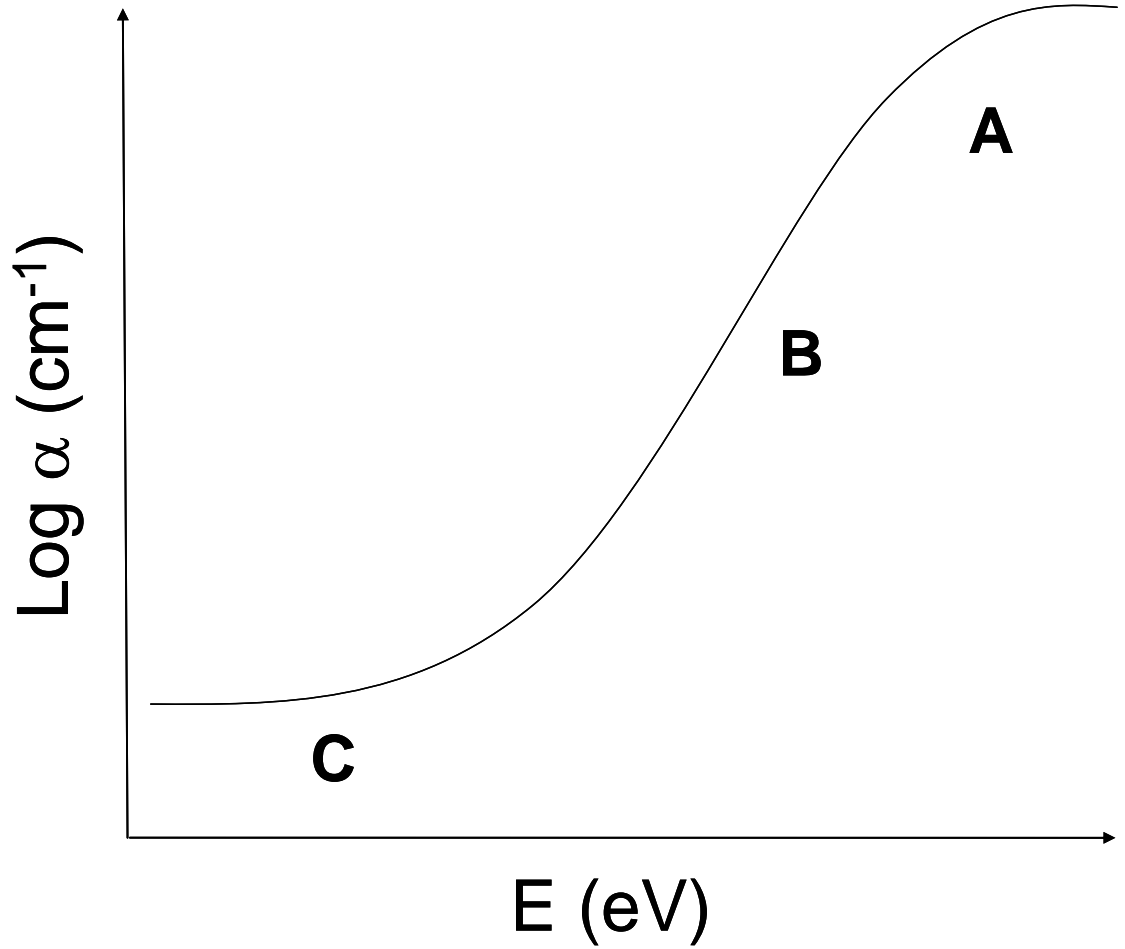
Figure 11. Sketch of the absorption coefficient as a function of energy as collected by CPM. Absorption in the higher energy range is due to band/band transitions, in the mid energy range due to the band tail/band transitions, and the absorption in the lower energy range is due to defect/band transitions and is a measure of the defect states of the film. The Urbach slope is found in region B and gives a measure of the width of the band tails.

The Constant Photocurrent spectrum is measured with the sample residing in a vacuum chamber capable of in situ annealing of the film. Light from an LPS 220 adjustable lamp power supply with a tungsten halogen source passes through an Oriel 77250 monochromator with a stepper motor. After being mechanically chopped the light is focused onto the sample and the resulting photocurrent is detected with an SR530 lock-in amplifier and Ithaco 564 Low Noise Pre-amplifier. All measurements were performed at room temperature and nominal vacuum (~50 mTorr). A beam splitter sends ten percent of the monochromatic light to a photodiode that records the incident light intensity.

3.e.- High Resolution Transmission Electron Microscopy

High resolution transmission electron microscopy (HRTEM) was used to verify the presence of nanocrystalline inclusions in the mixed phase films using thermophoresis to drive particles into or away from the depositing film.[64] In order to image the bulk of the film, samples that are several hundred nm thick films were cross-sectioned using a small angle cleaving technique (SACT), as ion milling can affect the structure of the films. Dark-field imaging using a Philips CM30 TEM operating at 300 kV highlights as bright spots those crystalline regions that satisfy the Bragg diffraction condition for the location of the objective aperture.[11] Focal series imaging, where the image is deliberately detuned from constructive interference, confirms that the fringes observed arise from crystalline regions and are not an experimental artifact.

The particle size distribution and the particle crystallinity were studied by transmission electron microscopy (TEM) analysis where the silicon nanocrystals are collected on a stainless steel mesh, with no silane plasma present in the second CCP chamber. Particles are found to be crystalline, with a monodisperse size distribution. The typical standard deviation of the particle size distribution is usually ~15% of the peak size.

3.f.- RAMAN Spectroscopy

The crystalline and amorphous content of the mixed phase a/nc-Si:H films is characterized via Raman spectroscopy. In a Raman process monochromatic light interacts with a material's phonons, and the inelastic scattering induces a shift in the energy and therefore the wavelength of the light. The efficiency of this process is very small and the vast majority of the light experiences Rayleigh scattering with no shift in the photon energy. The Raman scattering involves either energy absorption or emission, characterized as Stokes and anti-Stokes Raman scattering, respectively. The magnitude of the energy shift provides information about the phonon modes of the system. Silicon atoms in an amorphous matrix will have different vibrational states than silicon within a crystallite inclusion. Examination of the Stokes shifts of the light reflected from a solid can discriminate between the amorphous and crystalline phases, and the relative integrated intensities provide quantitative determinations of the material's crystalline and

45

amorphous content, contingent on assumptions regarding the oscillator strength of the silicon in the crystalline or amorphous phases.

Raman spectra are obtained using a Witec Alpha 300 R confocal Raman microscope equipped with a UHTS 200 spectrometer using an Argon ion excitation laser of wavelength 514.4 nm at a power of 5 mW focused to an area of 700 nm diameter. The maximum power is always kept below 15 mW to avoid laser crystallization of the film that will provide a false value for the crystalline fraction.[65] This laser induced crystallization is observed in a-Si:H; care must be taken with the laser power as this effect is enhanced when silicon crystalline clusters are near the surface of the film.[66] The depth of field of the confocal microscope is approximately 500 nm, comparable to or larger than the thickness of the films being measured. By varying the depth of field for thicker films, we have confirmed that the observed nanocrystalline signal is characteristic of the bulk of the film. The Raman spectra presented are acquired using a low incident laser power to avoid any shifts of the peak position due to thermal annealing of the sample. Raman spectra are recorded from several different locations along the film surface, to ensure that the results are characteristic of the material and do not reflect a local fluctuations in nanocrystal concentration. The micro-Raman apparatus allows us to sample small areas between the deposited electrodes, eliminating additional background, and reducing the effect of atmospheric moisture.

Commercial curve fitting software is used to fit the measured Raman spectra with Gaussian curves in order to calculate the crystalline fraction. The broad peak observed at 480 cm^{-1} reflects the TO mode of the a-Si:H material while bulk crystalline silicon has a narrow peak at 520 cm^{-1}. The crystalline fraction is defined as

$$X_c = I_{518}/(I_{518} + \lambda\, I_{480})$$

where I_{480} is the area under the peak at 480 cm^{-1} and I_{518} is the area under the peak at 518 cm^{-1}. The nanocrystallites incorporated into the mixed phase amorphous silicon exhibits a Raman peak downshifted to 518 cm^{-1}.[67-68] There is also evidence for a Raman peak at 500 cm^{-1} in the film with a high nanocrystalline concentration, which has been interpreted as arising from the grain boundary region surrounding the nanocrystalline inclusions.[69] The ratio of the Raman backscattering cross-section factor λ is determined from comparisons of Raman spectra for bulk crystalline silicon to pure a-Si:H films; values frequently cited in the literature range from $\lambda = 0.8$ to $\lambda = 0.88$. When we use a cross-section factor λ of 0.8 - 0.88, the calculated X_c increases by a small amount. As we are interested in comparing the effects of a relative increase in nanocrystal concentration, and given that the role that quantum confinement plays on the Raman backscattering cross section is not well understood, we have made the simplifying assumption of $\lambda = 1.0$ for our Raman data.

4.- Experimental Results

The structural, optical and electronic properties of mixed phase a/nc-Si:H thin films are now discussed. We begin with considerations of mixed phase films synthesized in a single PECVD chamber, where the silicon nanocrystallites are generated in the same plasma from which the surrounding a-Si:H matrix is formed. In the single chamber films, the nanocrystalline content in the film is controlled by a thermal gradient imposed across the plasma. The material properties of these films are compared to those deposited in a dual chamber co-deposition system, where the nanocrystallites are formed in one plasma deposition system, and are then injected into a second chamber where the a-Si:H is grown. Here again, the concentration of nanocrystalline inclusions in the resulting a/nc-Si:H is determined by thermophoretic forces across the plasma in the second chamber. Finally, the properties of undoped a/nc-Si:H films deposited in the dual chamber system are compared to n-type doped mixed phase films.

4.a.- Single Chamber Deposited Mixed Phase Films

The central premise of the single chamber studies is that the silicon nanocrystallites are formed within the silane plasma and are then transported to the growing film surface. In order to ascertain whether this does indeed occur, or if nanocrystallites are created by solid-state nucleation at the growing film substrate on which the a-Si:H is synthesized, studies of the plasma conductance were performed by

the Kortshagen lab. The current and voltage characteristics of the plasma were examined simultaneously using a Picoscope 212-100 oscilloscope. The current was monitored by a Pearson 2877 wideband current probe and the dividing capacitor voltage probe (1/100) recorded the voltage. Both the current and voltage display a sinusoidal time dependence, with the phase difference between the current and voltage signals, determined by measuring the time lag between the peaks of the signals, being very sensitive to changes in the plasma conditions. There is a sharp rise in phase difference and dissipated plasma power observed when a silane plasma is operated under conditions that yield nanocrystalline formation.[70-71] In contrast, no such change is found when only hydrogen and helium gases (that is, no silane which is necessary for silicon deposition) is used at the same total chamber pressure as with silane deposition.[40] The results for the silane plasma reflects an increase in the plasma resistance at high gas chamber pressures, and is most likely due to the formation of particles within the plasma, consistent with studies of other laboratories.[72]

Transmission Electron Microscopy confirms that the particles in the plasma are susceptible to a thermophoresis force when a thermal gradient exists between the parallel plates in the capacitively-coupled PECVD reactor. The images in Figure 12 were acquired by Chris Perrey.[49] Mixed Phase a/nc-Si:H films deposited at 1450 mTorr were dark-field imaged using a Philips CM30 TEM operating at 300 kV. In dark-field images those crystalline regions that satisfy the Bragg diffraction condition for the location of the objective aperture appear as bright spots. Silicon nanocrystallites of average diameter of

5 nm are evident in the dark field image in Figure 12a for an a/nc-Si:H film deposited
with no temperature gradient between the substrate and RF electrodes (both maintained at
T = 523 K) during film synthesis. The growth conditions for the film dark-field imaged
in Figure 12b are identical, with the exception that a positive thermal gradient (grounded,
substrate electrode held at 523 K and the RF electrode unheated) obtained during
deposition. A positive gradient corresponds to the deposition electrode being at a higher
temperature that the RF electrode, and the resulting thermophoretic force would push
particles away from the deposition substrates. The film in Figure 12b, is amorphous and
does not contain crystallite material. This sensitivity to a thermophoresis effect on the
resulting film structure is consistent with observations reported for polymorphous Si:H.
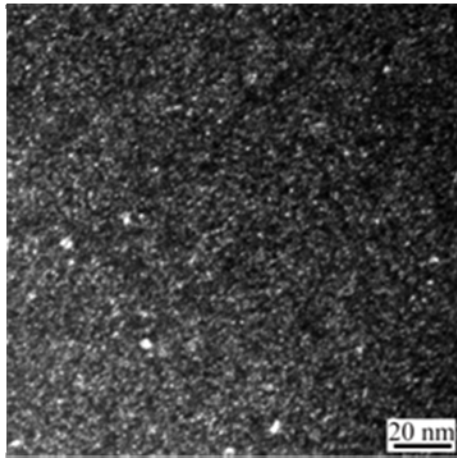
Figure 12a: Dark-field TEM image of an a/nc-
Si:H film deposited at 1450 mTorr with ΔT = 0.
Bright spots arise from Bragg diffraction from
nanocrystals roughly 5 nm in size.
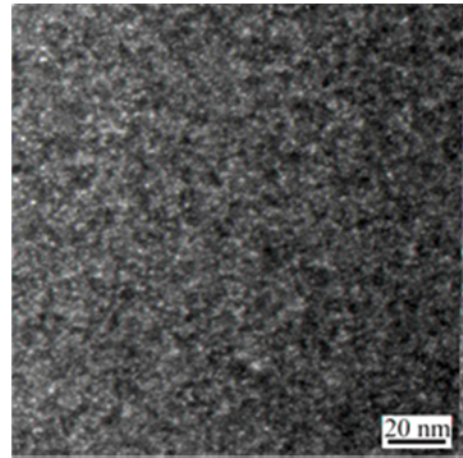
Figure 12b: Dark-field TEM image of an
a/nc-Si:H film deposited at 1450 mTorr
with ΔT > 0. No nanocrystals are evident.

50

The amorphous silicon matrix surrounding the embedded silicon nanocrystallites is also sensitive to thermophoretic forces, as reflected in measurements of the infra-red absorption spectra. Previous studies by other groups has identified the silicon-hydrogen vibrational modes at wavenumbers of 2000 and 2090 cm^{-1} as the bond-stretching modes of Si-H and Si-H$_2$ bonds respectively and have associated a higher absorption at 2090 cm^{-1} with lower quality materials that contain higher amounts of structural and electronic disorder.[42] Figure 13a plots the infra-red absorption spectra for the a/nc-Si:H films grown at a pressure of 360 mTorr and heavy hydrogen dilution (R = [H$_2$]/([H$_2$] + [SiH$_4$]) = 50) for the frequency range of 1900 to 2200 cm^{-1}. Films deposited under these conditions have a high concentration of silicon nanoparticles. The peak in the infrared spectrum shifts towards a wavenumber of 2090 cm^{-1} as the thermal gradient during deposition is reversed from its normal positive value (grounded deposition electrode hotter than the RF electrode) to a negative gradient (deposition electrode is cooler than the RF electrode).
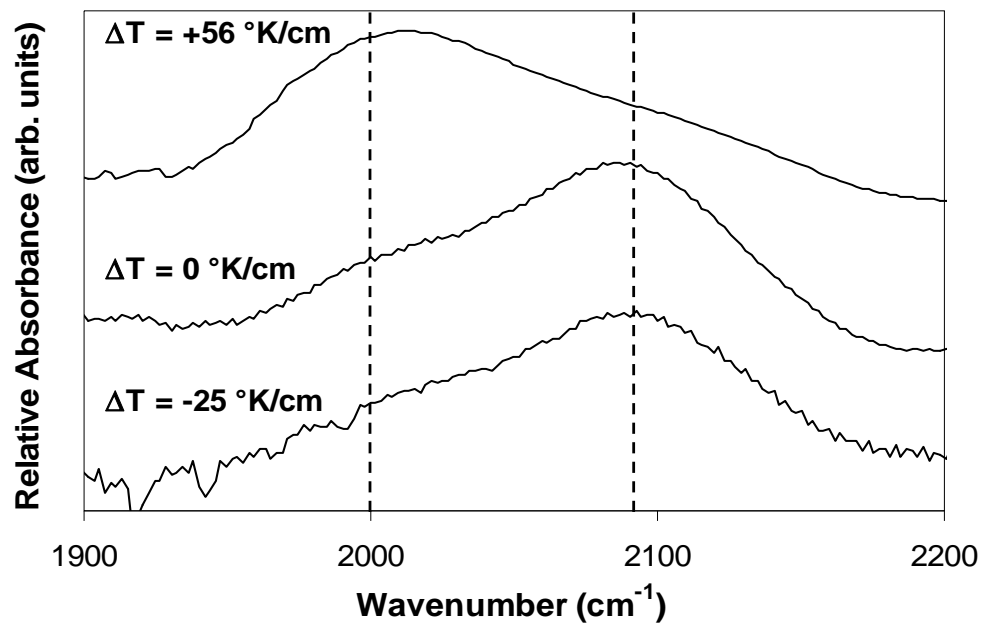
Figure 13a: Infrared absorbance of undoped silicon films deposited with a hydrogen dilution ratio of 50 and thermal gradients of +56, 0 and -25 °K/cm.
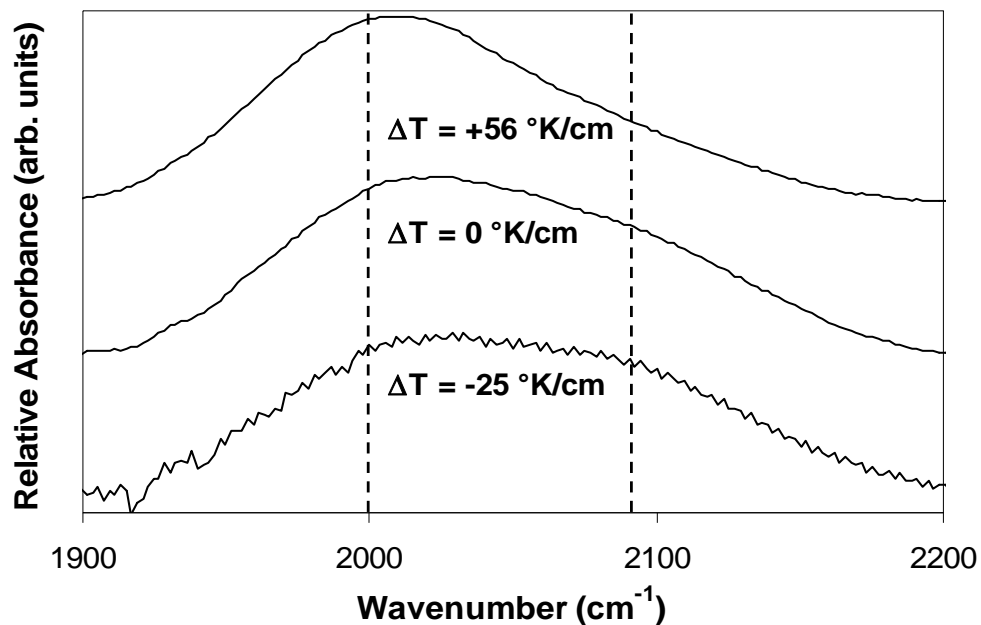
Figure 13b: Infrared absorbance of undoped silicon films deposited with no hydrogen dilution (R = 0) and thermal gradients of +56, 0 and -25 °K/cm.

In contrast, Figure 13b shows comparable infra-red abortion spectra for material deposited with no hydrogen dilution (R = 0). While the increase in infra-red absorption at 2090 cm^{-1} is less pronounced, it is still present, even under condition not conducive to nanocrystal formation within the silane plasma. These data indicate that there is a clear degradation on the structure of the amorphous silicon matrix surrounding the nanocrystalline inclusions in mixed phase a/nc-Si:H films when a thermal gradient is imposed, and the effect is most pronounced for a gradient orientation that would push particles toward the growing film surface.[24]

The optical properties of the films deposited when R = 0 were measured using the Constant Photocurrent Measurement (CPM) technique, as shown in Figure 14. There is a

slight increase in the Tauc optical gap from 1.6 eV for the Δ T = 56 K/cm film to 1.8 eV for the Δ T = - 25 K/cm film, as shown in Figures 15 and 16a. Similarly, plots of the optical absorption coefficient against photon energy (Figures 14 and 16b) reveal a slight broadening of the Urbach slope when the thermal gradient across the silane plasma during deposition is reversed from positive to negative. These films are only several hundred nm thick, and consequently the optical absorption data is partially obscured by Bragg thin film interference fringes. Nevertheless, the shift in the absorption edge with changing thermal gradient during deposition can be discerned.
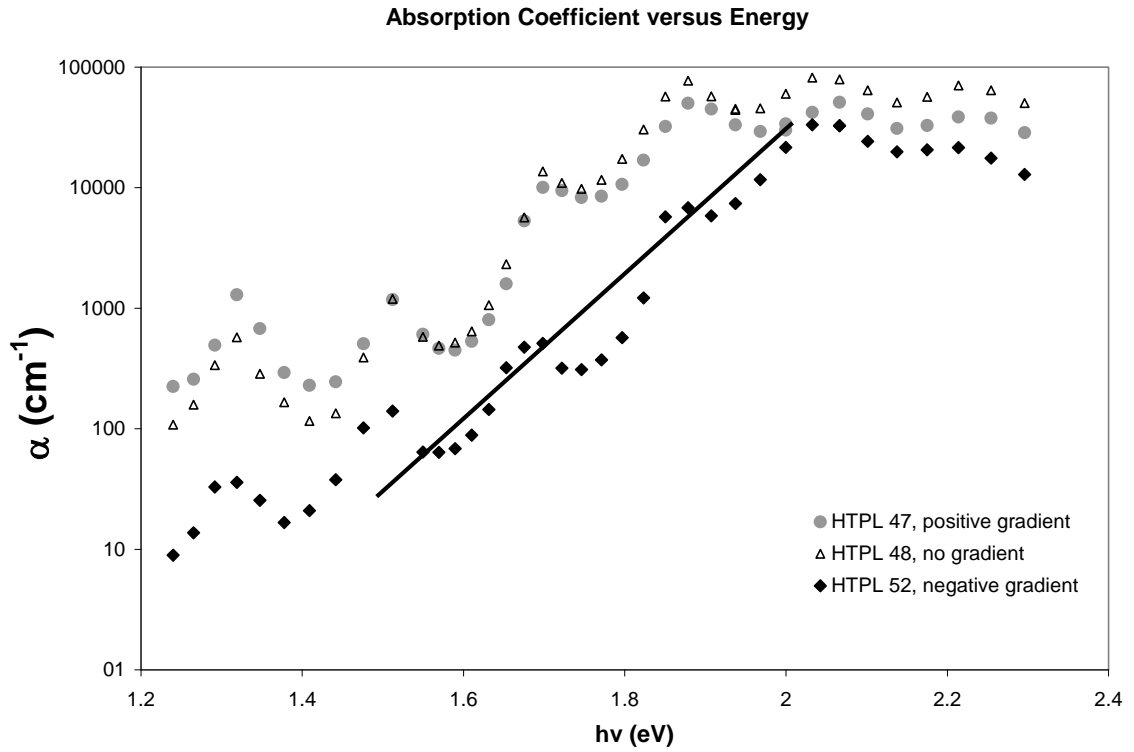
Figure 14.   Absorption coefficient versus energy for films deposited in the single chamber deposition system with R = 0.   The defect density can be seen in the lower energy region.
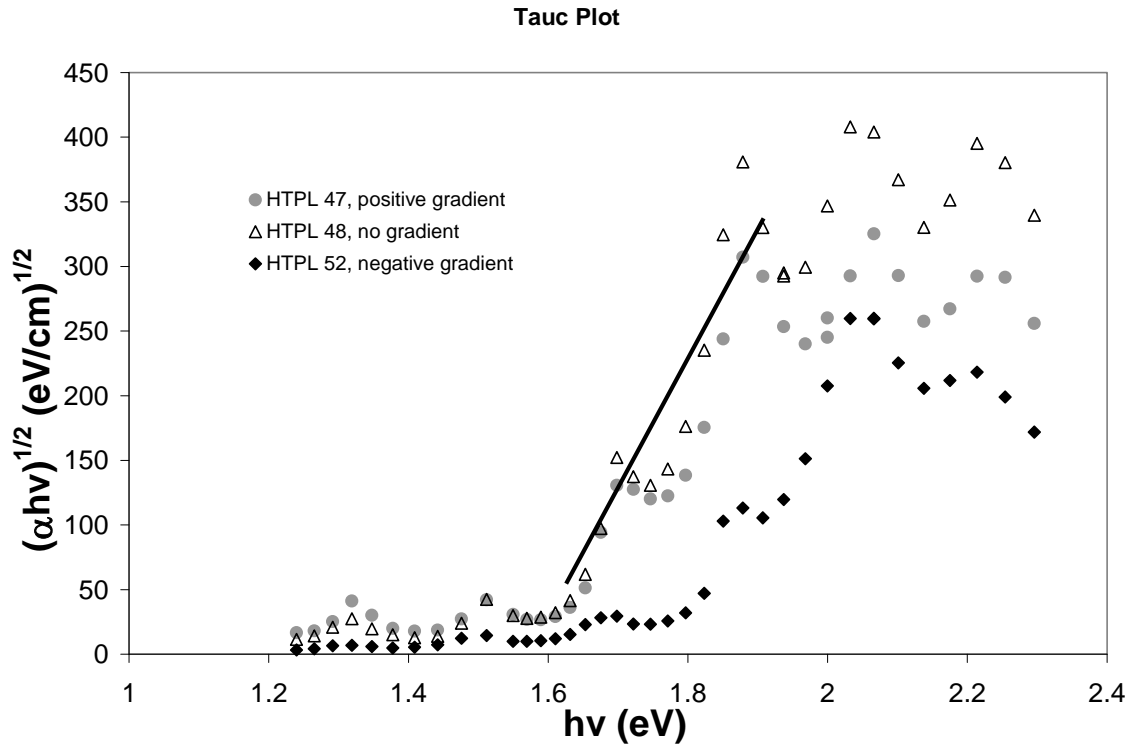
Figure 15. Tauc plot of films deposited in the single chamber deposition system with R = 0. The x-intercept of the fit of the linear portion is used to determine the optical gap of the films.

Tauc gap versus thermal gradient
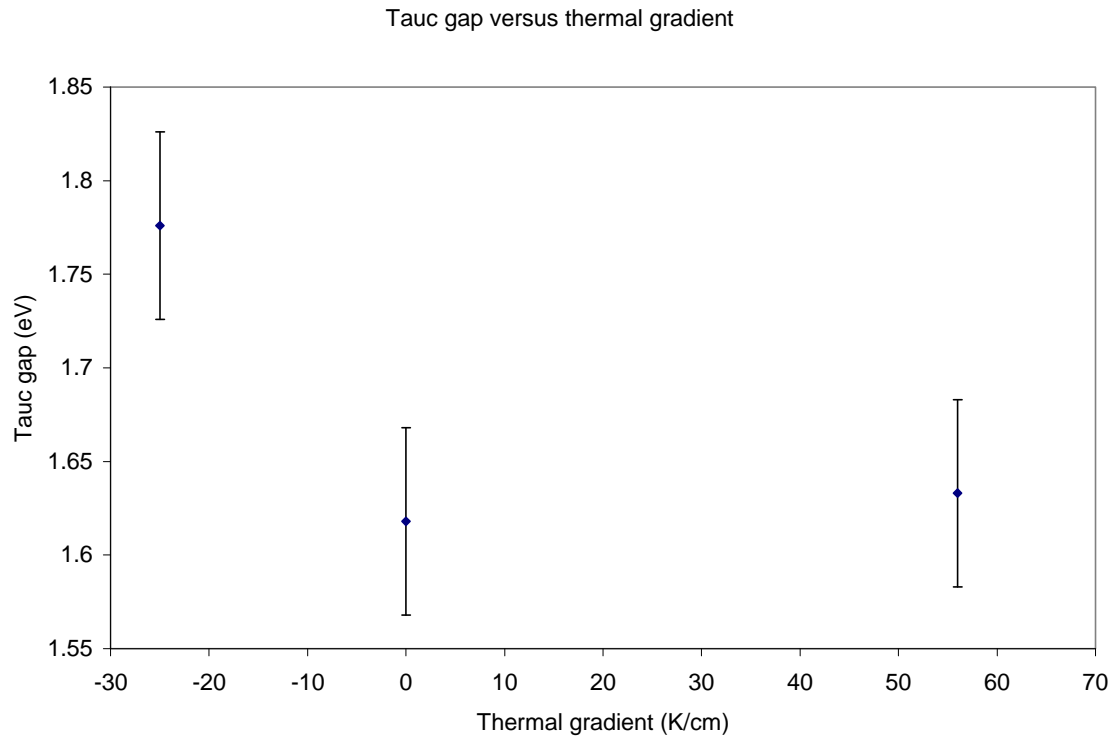
Figure 16a. The optical gap of the films increases when the thermal gradient is switched from a positive value to a negative value.

Urbach slope versus thermal gradient
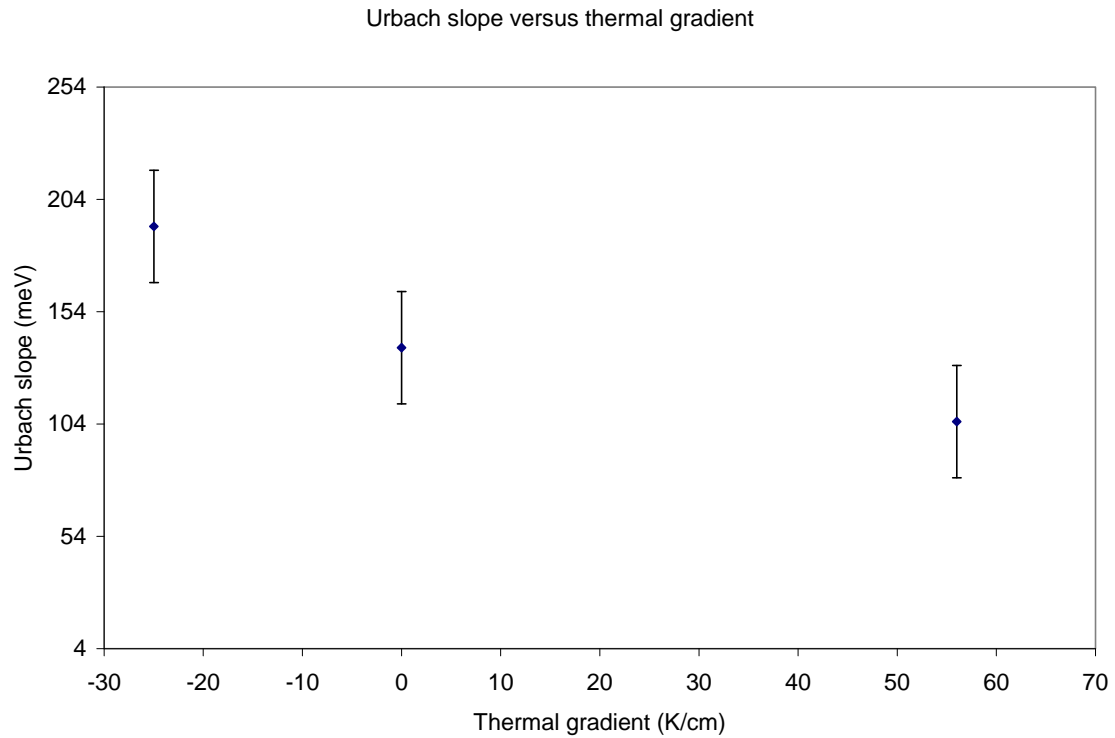
Figure 16b. There is a broadening of the Urbach slope with the switching of the thermal gradient from a positive value to a negative value.

The temperature dependence of the annealed (state A) dark conductivity for the films deposited without hydrogen dilution (R = 0), and for those deposited with a hydrogen dilution ratio R = 50 are shown in the Arrhenius plots in Figures 17 and 18, respectively. Both figures clearly indicate that both the dark conductivity magnitude and activation energy are sensitive to the thermal gradient present during deposition. The lowest conductivity is observed for films deposited with a negative thermal gradient, which tends to push any particles in the plasma towards the deposition electrode, suggests that the incorporation of these particulates has a deleterious effect on the resulting film's

electronic properties. The lower conductivity for the $\Delta T < 0$ a/nc-Si:H may be associated with a decrease in the structural and electronic quality of the a-Si:H matrix, reflected in the higher Si-H$_2$ content (see Figure 13b). The low-temperature activation energies for the a-Si:H films in Figure 17 are 0.89, 0.70 and 0.62 eV for $\Delta T = -25$, 0, and + 56 K/cm, respectively. The slight downward kink in the conductivity at higher temperatures is observed in undoped a-Si:H without nanocrystalline inclusions and is associated with thermal equilibration of the defect structure. The activation energies (0.72, 0.72 and 0.59 for $\Delta T = -25$, 0, and + 56 K/cm, respectively) for the R = 50 series (Figure 18) are less sensitive to the thermal gradient imposed across the silane plasma during film growth. However, the lowest dark conductivity values are observed for materials deposited with a thermophoretic force that would increase the density of nanoparticles incorporated into the growing film surface.

These results suggest that the optimal solution may be to separate the growth of the silicon nanocrystals from the synthesis of the surrounding a-Si:H matrix. Such a sensitivity of the dark conductivity for the R = 50 films to a thermophoresis effect is consistent with other studies of material deposited at higher pressures, where large scale nanocrystallites are known to be incorporated into the amorphous silicon matrix. That such similar behavior is found for the R = 0 films (Figure 17) is unanticipated and suggests that, even for very low silane partial pressures of only 5 mTorr (with the total gas pressure composed of ~5 mTorr silane and ~95 mTorr of Helium for a total gas pressure of 103 mTorr), in the absence of heavy hydrogen dilution, particulates may be

present within the silane plasma that are large enough to be influenced by a thermal gradient.
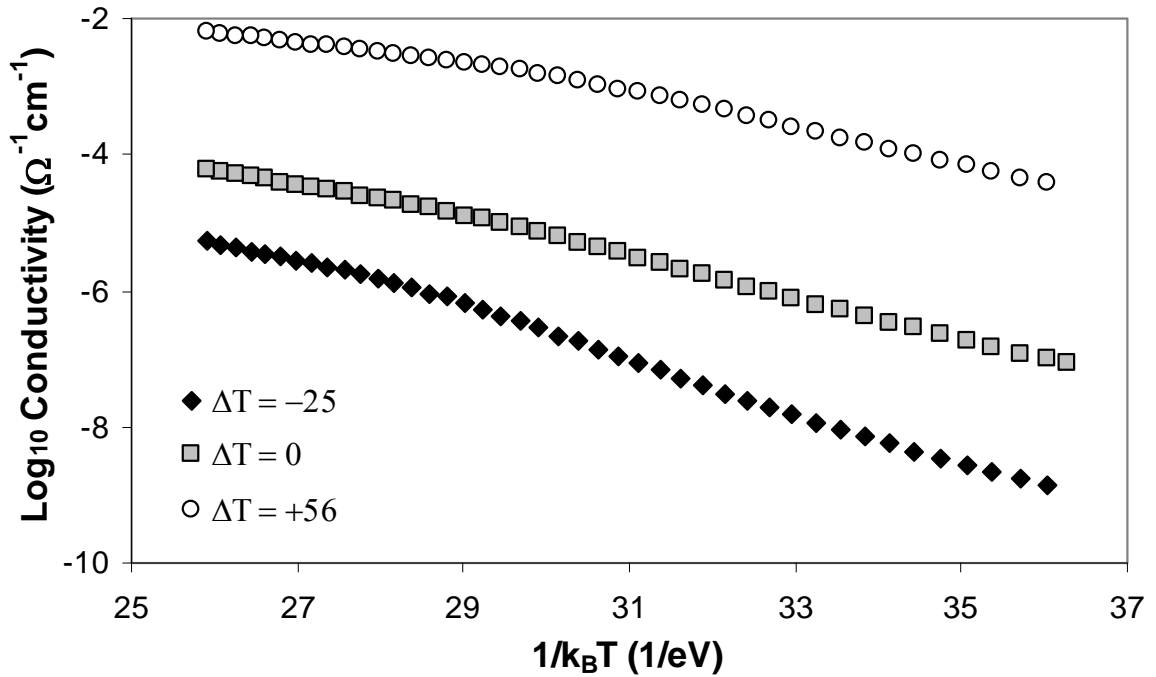
Figure 17: Arrhenius plot of the dark conductivity as a function of temperature in State A for the films deposited with a hydrogen dilution ratio of zero and thermal gradients of -25 (solid diamonds), 0 (shaded squares), and +56 °K/cm (open circles).

Figure 18: Arrhenius plot of the dark conductivity as a function of temperature in State A for the films deposited with a hydrogen dilution ratio of 50 and thermal gradients of -25 (solid diamonds), 0 (shaded squares), and +56 °K/cm (open circles).

The lowest conductivity is observed for films deposited with a negative thermal gradient, which would tend to push any particles in the plasma towards the deposition electrode, would indicate that the incorporation of these particulates has a deleterious effect on the resulting film's electronic properties. However, studies of the light-induced degradation of the photosensitivity and dark conductivity (the Staebler-Wronski effect) described below, suggest that films deposited with a negative thermal gradient may have advantages for solar cell applications.
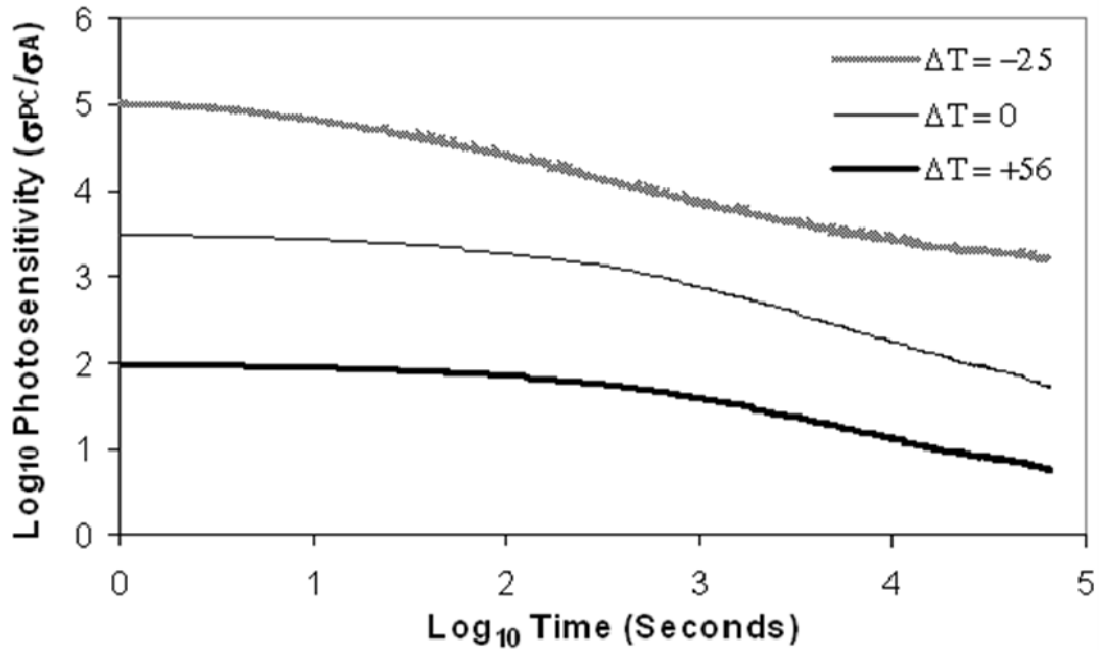
Figure 19: Plot of the photosensitivity (the photoconductivity normalized by the State A conductivity) as a function of time for the films deposited with a hydrogen dilution ratio of zero and thermal gradients of -25 (shaded line), 0 (thin line), and +56 °K/cm (bold line).

The dark conductivity as a function of exposure time with 100 mW/cm^2 of heat-filtered white light from a W-Ha lamp has been investigated. Following extended light soaking, the material is in State B. As summarized in Table 1, for the R = 0 series, the Staebler-Wronski effect is weakest for the film deposited with a negative thermal gradient across the silane plasma. The smaller Staebler-Wronski effect may be due to the lower initial conductivity of this material. However, despite the fact that the $\Delta T = -25$

K/cm film has a lower initial defect density (as determined by CPM) than the $\Delta T = + 56$ K/cm film, its initial photoconductivity value, measured with white light illumination at room temperature as described above, is the lowest of the series, also listed in Table 1. The combination of a slightly lower photoconductivity and a much lower dark conductivity in state A results in the $\Delta T = - 25$ K/cm film having a significantly higher photosensitivity (defined at the ratio of photoconductivity and state A dark conductivity). As shown in Figure 19, all three films in the $R = 0$ series display a degradation of the photosensitivity (a parameter relevant for photovoltaic applications) with light-soaking. However, even after extended illumination, the photosensitivity of the $\Delta T < 0$ film is at least two orders of magnitude larger than the initial starting value of the $\Delta T = + 56$ K/cm a-S:H film. These results of Figure 19 suggest that adjustment of the thermophoretic force during deposition may in fact lead to improvements in the resistance of photovoltaic devices to light-induced degradation.

All of the films in the $R = 50$ series have a weaker relative Staebler-Wronski effect when compared to the $R = 0$ films deposited under similar conditions. Interestingly, the $R = 50$ film deposited with $\Delta T = 0$ shows the largest light-induced degradation compared to the $\Delta T < 0$ and $\Delta T > 0$ films. While there is only a slight improvement in the resistance to the Staebler-Wronski effect for the pure a-Si:H films as a function of the thermophoresis effect, there is a marked difference when the $R = 0$ films are compared to the $R = 50$ series, as seen in Figure 20. While the dark conductivity of $\Delta T = +56$ °K/cm, $R = 50$ film is lower than that of the corresponding film in the $R = 0$

series by a factor of about 40 at 322 °K, the R = 50 film exhibits a much smaller degradation in the conductivity following approximately 20 hours of light exposure. As indicated in Figure 20, the State B conductivity for the R = 50 film is an order of magnitude higher than the corresponding state B of the R = 0 film. The R = 50 film even shows a small increase in the photoconductivity (termed persistent photoconductivity) during the first hour of light exposure, and for longer exposures displays a significantly slower photoconductivity decay, compared to the R = 0 film. These results suggest that the hydrogen dilution of the silane plasma during deposition plays an important role in reducing the degradation associated with the SWE, although it is not yet clear what the underlying mechanisms are.
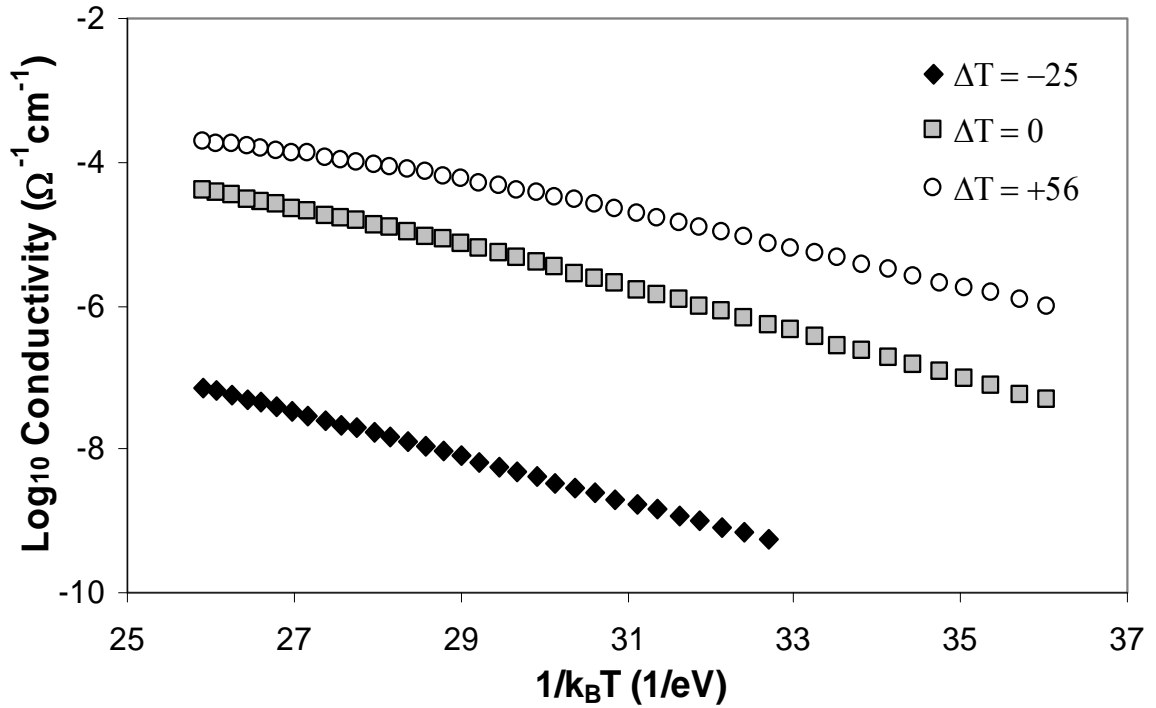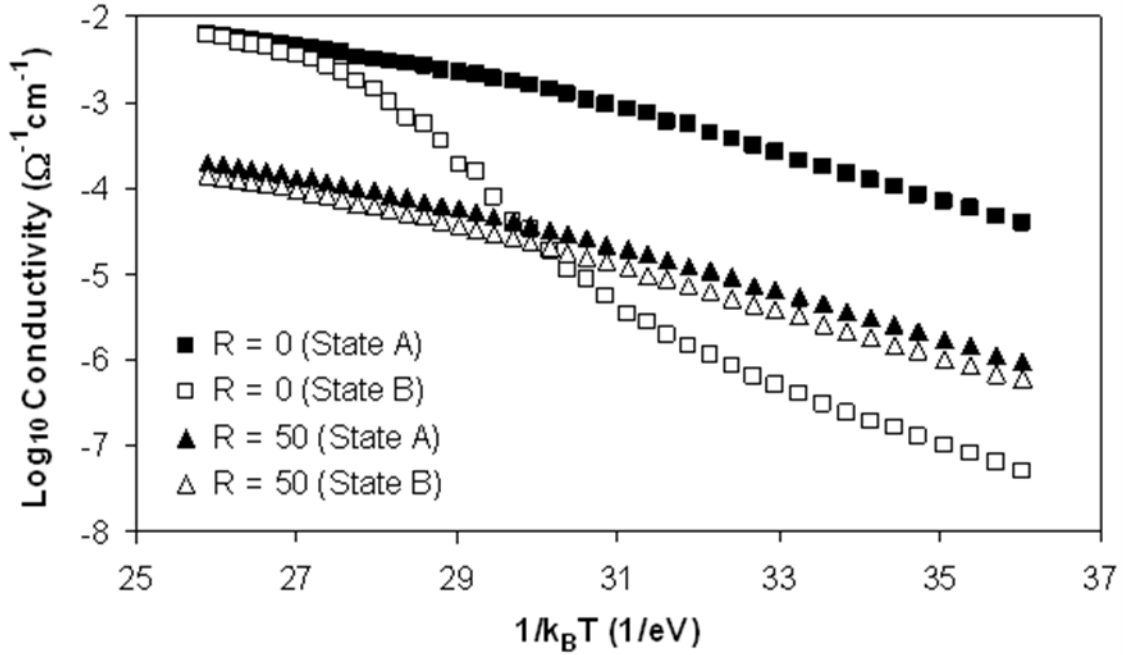
Figure 20: Arrhenius plot of the dark conductivity as a function of temperature for the films deposited with a thermal gradient of +56 °K/cm and hydrogen dilutions ratios of zero (squares) and 50 (triangles). Data are shown for both State A (solid symbols) and State B (open symbols).

The difference between activation energies obtained from the temperature dependence of the conductivity and thermopower, denoted as E_σ and E_S respectively has been measured for these films. This difference has been attributed to the influence of long-range potential fluctuations and compositional morphology present in amorphous semiconductors, causing the mobility edges to vary spatially. As such, this activation energy difference may serve as a measurement of an amorphous semiconductor's long-range electronic disorder. The activation energy difference increases from E_σ - E_S = 0.19

eV to E_σ - E_S = 0.22 eV for the Δ T = +56 °K/cm and Δ T = 0 films in the R = 0 series, and from E_σ - E_S = 0.17 eV to E_σ - E_S = 0.22 eV for the R = 50 series. The thermopower of the ΔT = -25 °K/cm films could not be measured due to their high impedance. The small increase in the activation energy difference when ΔT = 0 is within the experimental error for these measurements, leaving open the question as to whether or not there is a real sensitivity of the activation energy difference with the sign of the thermal gradient.

In summary, the properties of a-Si:H films as a function of a controllable thermal gradient applied across the silane plasma during deposition have been investigated, under both nominal a-Si:H growth conditions and for when nanoparticles form in the plasma. Despite the fact that these films with R = 0 were synthesized at very low silane partial pressure without hydrogen dilution, there is a striking sensitivity of the resulting film properties to a thermophoretic force during film growth, consistent with particulates forming within the plasma even under ideal deposition conditions. Displaced-aperture dark-field (DADF) imaging has been employed to survey the crystalline material in a nominally a-Si:H sample (R = 0) deposited at 250 mTorr and a positive thermal gradient. These results suggest that if any crystallites are present they are likely smaller than ~1 nm. That such small crystallites may reside within nominally homogeneous a-Si:H films may lead to a renewed interest in various experimental characteristics of this technologically important material.

Hydrogen Dilution (R)	ΔT (°K/cm)	E_σ (eV)	M_{IR}	σ_A (Ω^{-1} cm^{-1})	σ_B (Ω^{-1} cm^{-1})	σ_{ph} (Ω^{-1} cm^{-1})
0	+56	0.62	0.25	4.5×10^{-4}	1.1×10^{-6}	2.6×10^{-3}
0	0	0.70	0.42	1.4×10^{-6}	9.0×10^{-9}	4.6×10^{-4}
0	-25	0.89	0.50	3.1×10^{-8}	2.6×10^{-9}	1.5×10^{-4}
50	+56	0.59	0.59	1.1×10^{-5}	6.3×10^{-6}	2.8×10^{-5}
50	0	0.72	0.72	8.1×10^{-7}	1.1×10^{-8}	1.4×10^{-4}
50	-25	0.72	0.72	8.1×10^{-10}	3.4×10^{-10}	1.5×10^{-7}

Table 1: Measured values of E_σ, M_{IR}, state A and B dark conductivity σ_A, and σ_B (the values of σ_A and σ_B are measured at 361 °K) and photoconductivity σ_{ph} at 300 K for the films deposited at varying thermal gradients.

4.b.- Dual chamber using Thermophoresis

The results of the preceding section found that the conductivity of the amorphous semiconductor films decreases as more particles were incorporated into the film. The changes in film properties following extended illumination indicate that there is a benefit to introducing nanocrystalline particles into the amorphous silicon matrix. The a/nc-Si:H films showed a significant reduction of the SWE while at the same time having a conductivity that was greater than the conventional amorphous silicon after light exposure, as illustrated in Figure 20. The conditions under which the a-Si:H matrix are deposited in the PECVD system in Figure 5 are very far from those typically employed to produce high quality a-Si:H. These deposition conditions were chosen in order to facilitate the formation of silicon nanoparticles in the plasma. A possible alternative approach would be to synthesize the nanoparticles in one plasma chamber, and then inject these particles into a second PECVD system, where a-Si:H is grown under conditions more typically employed by the semiconductor industry. In this section we describe the properties of mixed phase a/nc-Si:H films deposited in such a dual chamber co-deposition system, where the concentration of silicon nanocrystals is again controlled by a thermophoretic force.

The influence of the thermal gradient between the parallel plates in the second CCP chamber on the incorporation of silicon nanocrystals into the a-Si:H film is evident in high resolution transmission electron microscopy images, shown in Figure 21.[73-74]

Several hundred nm thick a/nc-Si:H films were deposited onto crystalline silicon wafers, which were then cross-sectioned via cleaving in order to image the bulk film. The sample imaged in Figure 21a were deposited with a positive thermal gradient, which tends to push any particles away from the growing film surface, while the film shown in Figure 21b were grown with a negative thermal gradient. These TEM images were obtained by Julia Deneen. Crystalline inclusions are clearly seen in Figure 21b but not in Figure 21a, confirming the sensitivity of particle incorporation to a thermophoresis force across the silane plasma in the second chamber. Focal series imaging confirms that the lattice fringes in Figure 21b are not microscope artifacts.
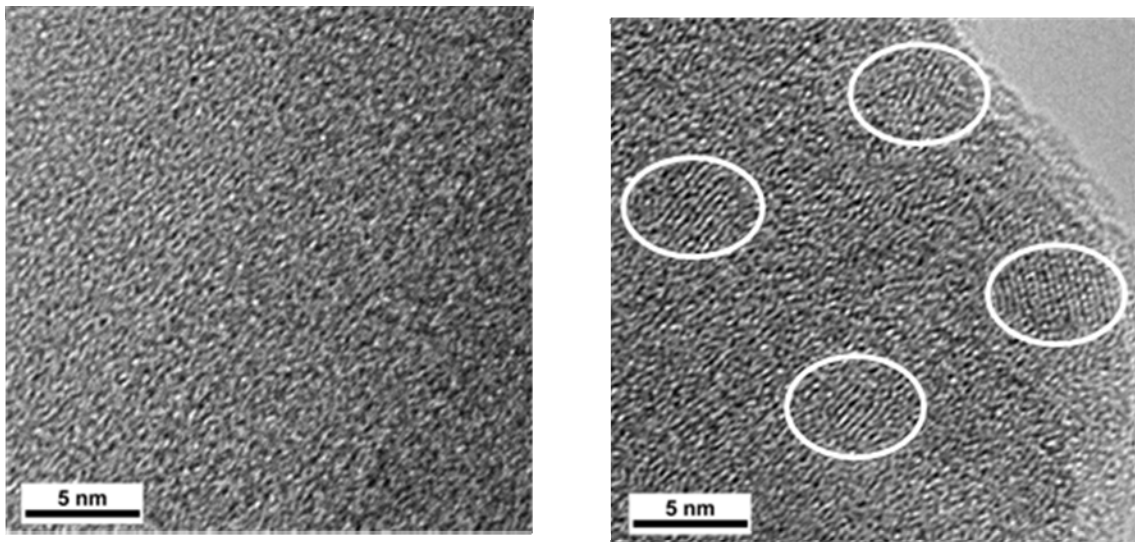
Figure 21. HR-TEM images confirm that the thermal gradient across the plasma directs the nanocrystals into the film or away from the film. In Figure 21a a-Si:H grown with Δ T > 0 – no particles are found in the film. Figure 21b shows a/nc-Si:H deposited when Δ T < 0 and nanocrystals are found to be present in the amorphous matrix.

Figure 22 compares the temperature dependence of the dark conductivity of a/nc-Si:H in the annealed state A and following two hours of illumination with 100 mW/cm^2 of heat-filtered white light from a W-Ha lamp (state B) as a function of the thermal gradient applied across the silane plasma during film growth. Chrome electrodes with a separation of 2 mm (which yielded linear current-voltage characteristics) were evaporated onto the 500 nm thick a/nc-Si:H films. Measurements were performed following annealing at 175°C for two hours under vacuum to remove any effects of prior light exposure or surface adsorbates. The State A conductivity of the $\Delta T > 0$ (Figure 22a) and $\Delta T < 0$ (Figure 22c) films are nearly identical, while a/nc-Si:H deposited with $\Delta T = 0$ (Figure 22b) shows an enhancement of nearly an order of magnitude in its state A dark conductivity. The increase in the dark conductivity following illumination has been observed in multilayer a-Si:H films consisting of alternating layers of n-type and p-type doped a-Si:H.[75] This "persistent photoconductivity" in Figure 22b is removed upon annealed. This film even in State A shows considerable curvature in the Arrhenius plot, unlike the $\Delta T > 0$ and $\Delta T < 0$ films. In state B, the dark conductivity of the a/nc-Si:H film grown with $\Delta T > 0$ (which would tend to push particles away from the growing film surface) decreases by nearly an order of magnitude, but is still higher than the state A dark conductivity of the a-Si:H film deposited without nanoparticles injected into the silane plasma.

The increase in dark conductivity when $\Delta T = 0$, compared to a/nc-Si:H grown with $\Delta T > 0$ suggests that the addition of nanoparticles improves the conductivity of the a/nc-Si:H film. However the observed decrease in conductivity between a/nc-Si:H deposited with $\Delta T = 0$ and $\Delta T < 0$ (where the thermophoretic force would increase the nanocrystalline content) suggests that there is a limit to the improvement made possible by the incorporation of these particles.

Conductivity vs. Temperature
$\Delta T > 0$ with nanoparticles

Figure 22a. Arrhenius plot of conductivity vs. inverse temperature of thin film grown with nanoparticle inclusions and a positive thermal gradient, which tends to push nanoparticles away from the growing film surface. Filled squares represent the annealed State A, when the film is in its annealed state, and open squares represent the films in State B, after the film has been light soaked, dark conductivities.

Conductivity vs. Temperature
ΔT=0 with nanoparticles

Figure 22b. Arrhenius plot of conductivity vs. inverse temperature of thin films grown

with nanoparticle inclusions and no thermal gradient.   Filled squares represent the

annealed State A, when the film is in its annealed state, and open squares represent the

films in State B, after the film has been light soaked. This material exhibited a small but

definite enhancement in the dark conductivity (termed a persistent photoconductivity)

following illumination, that was reversed upon annealing.

Conductivity vs. Temperature
ΔT<0 with nanoparticles

Figure 22c. Arrhenius plot of conductivity vs. inverse temperature of thin films grown with nanoparticle inclusions and a negative thermal gradient. Filled squares represent the annealed State A, when the film is in its annealed state, and open squares represent the films in State B, after the film has been light soaked.

It appears that thermophoresis is not the optimal method for controlling the nanoparticle concentration. For each of the thermal gradient conditions, we have also grown a-Si:H films where the RF power to the particle tube is turned off, and with no silane flowing through this first chamber (but with a flow of 50 sccm Ar maintained). When the plasma is not ignited in the particle synthesis reactor, no nanoparticles are observed in the a-Si:H films deposited in the second CCP chamber. Nevertheless, as shown in Figure 23 the dark conductivity of these a-Si:H films were found to be sensitive to the thermal gradient present during deposition, with a positive thermal gradient, corresponding to the normal deposition configuration of a heated grounded electrode on which the substrates reside and an unheated RF electrode, exhibited the highest conductance while $\Delta T < 0$ producing the most resistive material. The TEM images of these films showed no evidence of nanoparticle incorporation, indicating that any particles, if present, must be sub-nanometer in diameter. Particles this small are not expected to be sensitive to a thermophoresis effect, yet there is an observed variation in the electronic conductance of the a-Si:H due to the thermal gradient present during deposition. It should be noted that the substrate temperature of the grounded electrode in all three cases was maintained at 250°C, so that any observed changes are not due to variations in the deposition temperature.

Conductivity vs. Temperature
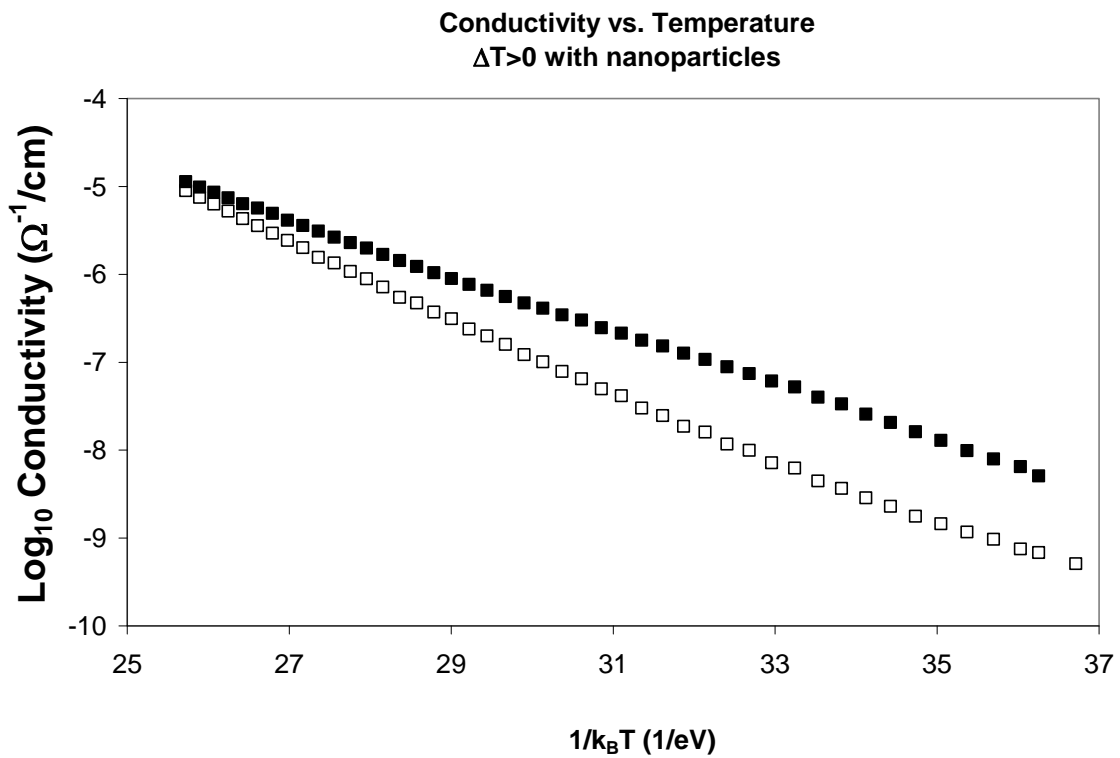**ΔT>0 without nanoparticles**
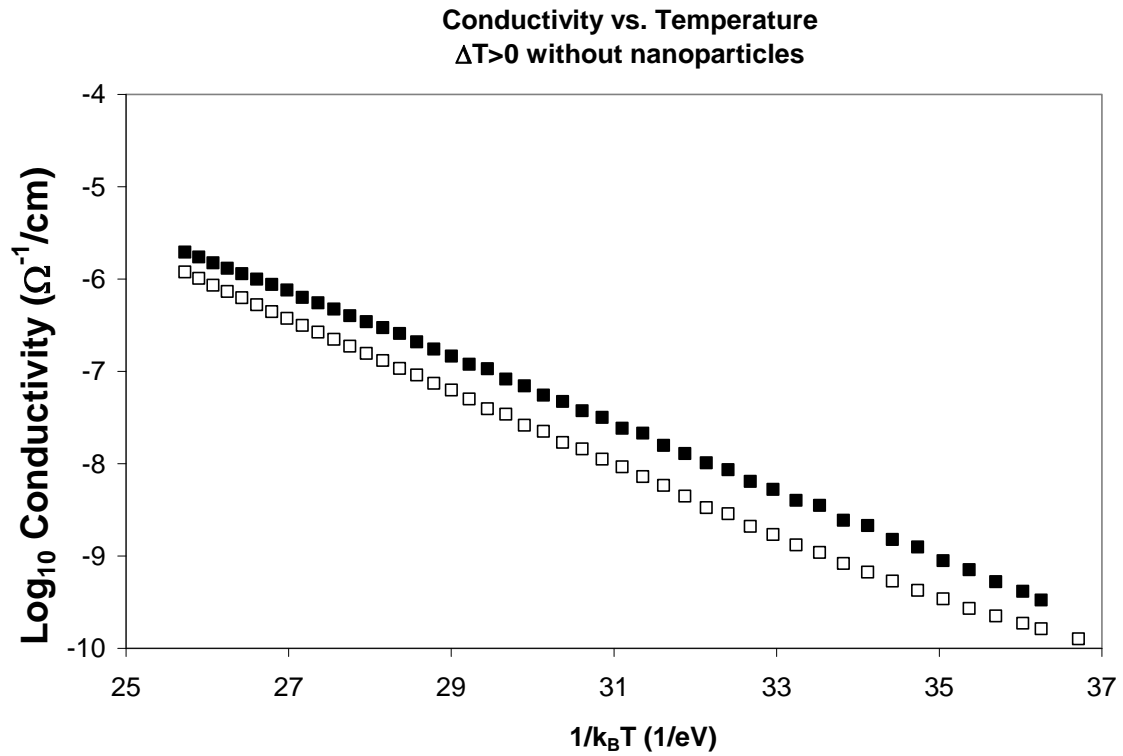
Figure 23a. Arrhenius plot of conductivity vs. inverse temperature of thin films grown without nanoparticle inclusions and a positive thermal gradient. Filled squares represent the annealed State A, when the film is in its annealed state, and open squares represent the films in State B, after the film has been light soaked.

Conductivity vs. Temperature
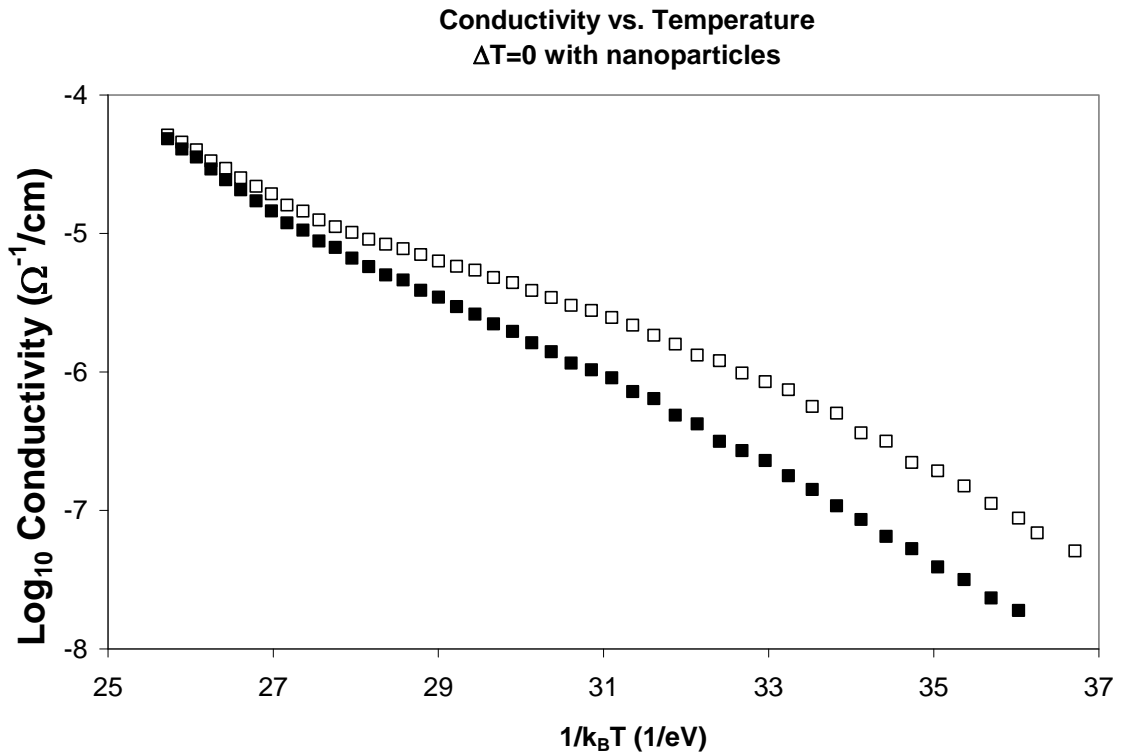**ΔT=0 without nanoparticles**
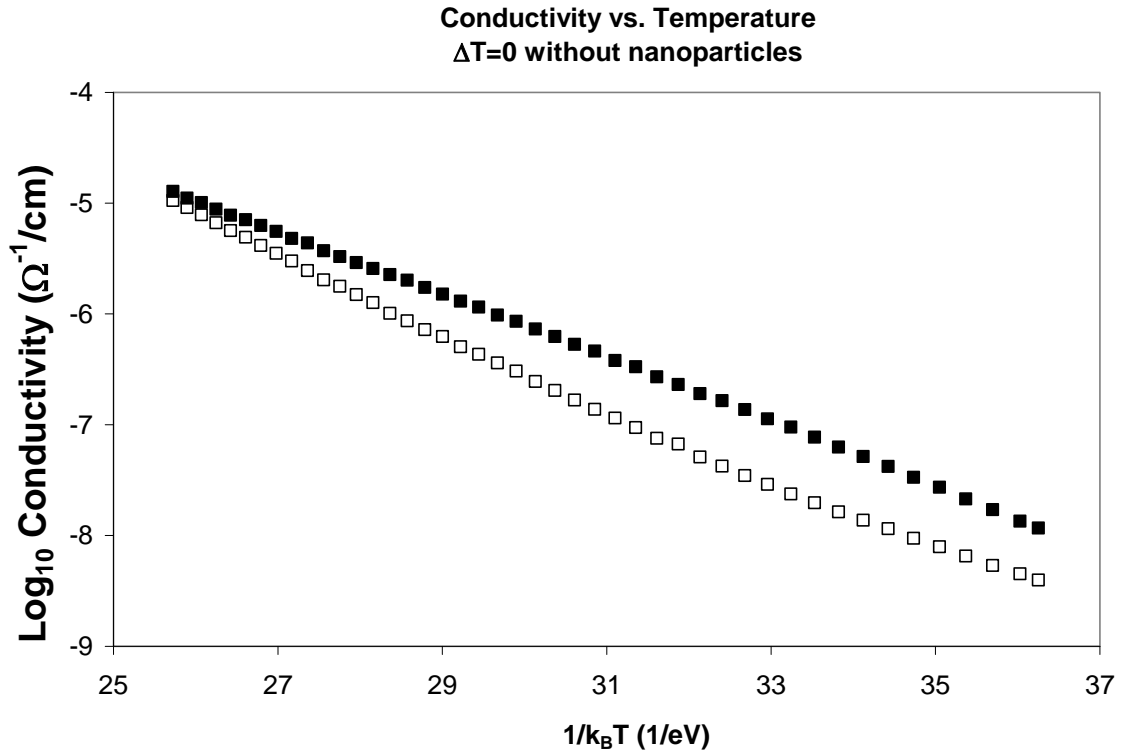
Figure 23b. Arrhenius plot of conductivity vs. inverse temperature of thin films grown without nanoparticle inclusions and no thermal gradient. Filled squares represent the annealed State A, when the film is in its annealed state, and open squares represent the films in State B, after the film has been light soaked.

Conductivity vs. Temperature
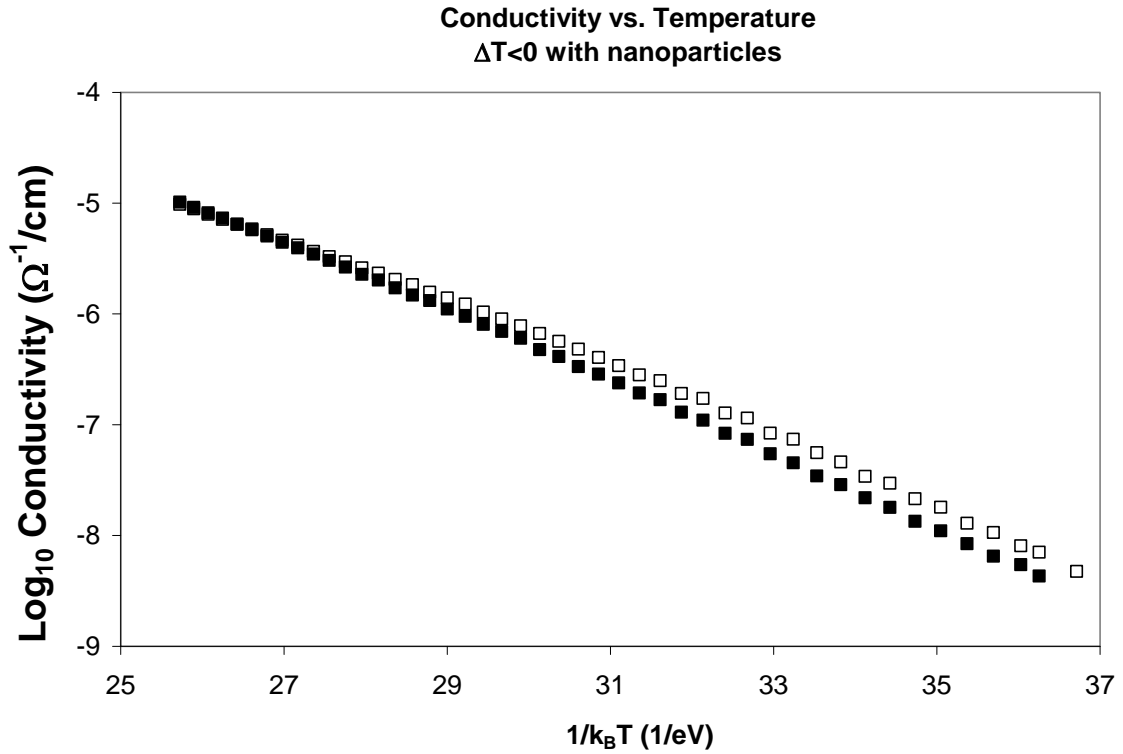**ΔT<0 without nanoparticles**
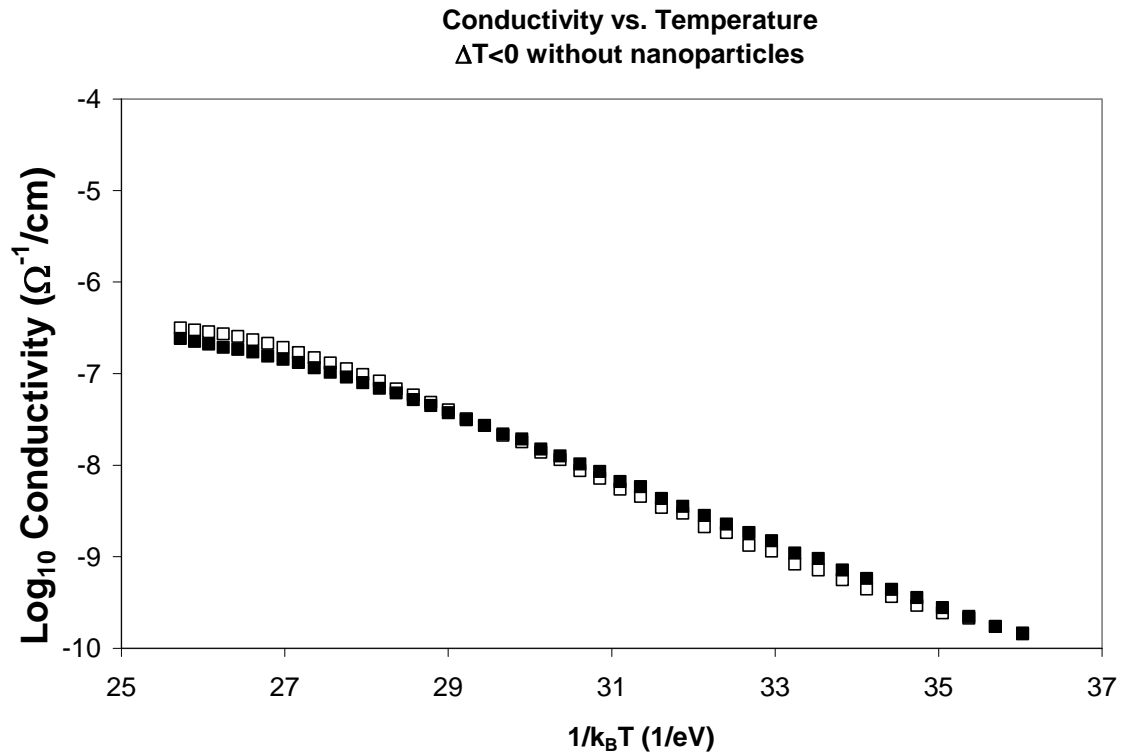
Figure 23c. Arrhenius plot of conductivity vs. inverse temperature of thin films grown without nanoparticle inclusions and a negative thermal gradient. Filled squares represent the annealed State A, when the film is in its annealed state, and open squares represent the films in State B, after the film has been light soaked.

As shown in Figures 22b and 24, the a/nc-Si:H film grown with $\Delta T = 0$ shows an unmistakable Persistent Photoconductivity (PPC) effect following 2 hours of light exposure. Also shown in Figure 24 are the results for an a-Si:H film also deposited with $\Delta T = 0$, but when the plasma production chamber turned off, so that no large scale nanoparticles are deliberately incorporated into the growing film. The film with no nanoparticles shows a normal SWE while there is an enhancement in the dark conductivity following illumination in the a/nc-Si:H sample. There is also a very slight PPC effect observed for the a/nc-Si:H film grown with $\Delta T < 0$ as well, which may be due to charge trapping at the silicon nanocrystal boundaries. The a/nc-Si:H deposited with $\Delta T > 0$ displays an initial photoconductivity of over 10^{-4} Ω^{-1} cm^{-1}, which decreases by nearly an order of magnitude following light exposure. In contrast, the photoconductivity for the $\Delta T = 0$ and $\Delta T < 0$ a/nc-Si:H is roughly 5×10^{-6} Ω^{-1} cm^{-1}, but for both films the photoconductivity does not decrease under light soaking.

Conductivity vs. Temperature
$\Delta T=0$
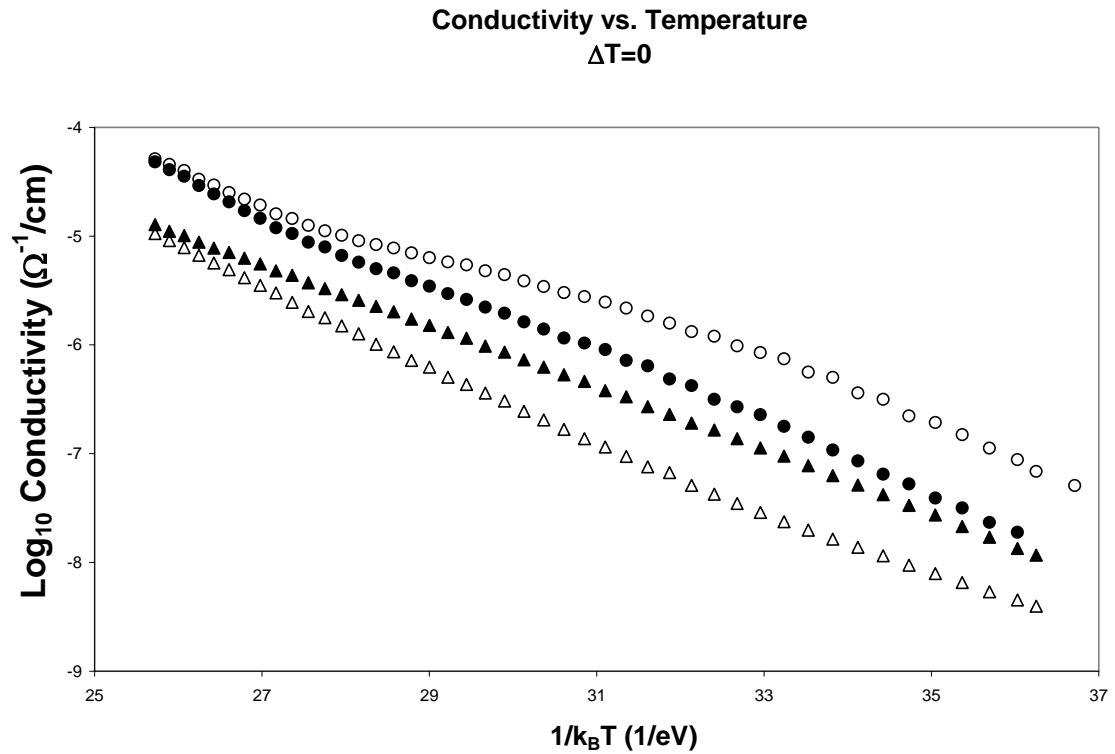
Figure 24. For a thermal gradient of zero, the conductivity increases when nanoparticles are introduced and the SWE is reduced. In this case, the mixed phase film displays PPC. Triangles represent the film without nanocrystallite inclusions whereas the mixed phase film is represented with circles. Filled symbols represent State A, when the film is in its annealed state, and open symbols represent the films in State B, after the film has been light soaked.

These results suggest that improvements in the material's properties would result if the nanoparticle concentration could be independently varied in films deposited with the same thermal gradient across the silane plasma. By modifying the configuration of the dual chamber deposition system, we are able to inject the silicon nanocrystallites through the top electrode. Introduction of the nanoparticles into the growing a-Si:H film surface is highly sensitive to convection by the inert carrier gas, and the concentration of nanoparticles in the a/nc-Si:H depends on the substrate's position relative to the injection point from the first chamber. The properties of a series of a/nc-Si:H films, grown following a modification of the deposition system in Figure 6, will form the basis of another student's thesis.

In summary, these measurements support the results found using the single chamber system, that is, the inclusion of nanocrystalline silicon particles have in some cases continued to reduce the SWE of the mixed phase a/nc-Si:H films, but also increased the conductivity as seen in Figure 24. An unexpected result was that even when nanocrystals were not being produced in the first chamber, the film properties are still sensitive to the thermal gradient across the plasma in the second chamber as seen in Figure 23. When the thermal gradient was changed from a positive to zero the SWE was decreased and the film was more conductive in state B. These results leads us to hypothesize that perhaps there are some sub-nanometer particles created in the plasma of the second chamber that are influenced by the thermophoretic force and affect the film's electrical properties. Monitoring the voltage as a function of current of the plasma in

80

order to determine whether there is an increase in resistance might indicate the formation

of sub-nanometer particles.

4.c.- Doped Mixed Phase Films

The results above indicate that the opto-electronic properties of hydrogenated amorphous silicon films are indeed sensitive to the inclusion of silicon nanocrystallites. While we are able to vary the concentration of nanoparticles by applying a thermophoretic force across the plasma during film deposition, this process also affects the properties of the surrounding a-Si:H matrix. Consequently the configuration of the dual chamber co-deposition system has been modified so that the concentration of nanoparticles injected into the second plasma deposition chamber can be varied by changing the conditions in the particle synthesis chamber. Knowing that the deposition rate of the film in the second chamber depends on the amount of residual silane that remains unreacted upon passing through the first chamber, films containing lower particle concentrations were produced by increasing the silane gas flow and thereby increasing the amorphous film portion of the mixed phase film. The achieved crystal fraction was determined using micro-RAMAN characterization. The properties of films deposited at a fixed thermal gradient ($\Delta T > 0$, which is the conventional configuration for a-Si:H synthesis) across the amorphous silicon deposition plasma are next described. The films investigated here are intentionally doped n-type by dynamically mixing PH_3 with the SiH_4 during particle formation and in the second capacitively-coupled chamber.

Raman spectroscopy confirms that control of the growth conditions in the particle synthesis chamber results in variation of the concentration of silicon nanocrystals. Figure 25 shows the Raman spectra for lightly doped (6×10^{-5} [PH_3]/[SiH_4]) a-Si:H deposited with the particle chamber turned off, and for a/nc-Si:H films grown with the particle chamber turned on, for a low and moderate concentration of embedded nanocrystals. The Raman spectra shows two lines in the region of $420 - 560$ cm^{-1}, a broad peak centered at 480 cm^{-1}, associated with the TO mode of amorphous silicon, and a sharp line at 520 cm^{-1} attributed to crystalline silicon. Fitting the area under these peaks, we find that $4.5 - 6.5$ sccm of silane flowing through the chamber yields low particle concentration corresponding to a crystalline silicon content of ~9% for low doped films and ~1% for highly doped films, while $2.5 - 4.5$ sccm of silane yields a high crystalline silicon content of ~30% for low doped films and ~3% for highly doped films.

The infrared absorption spectra for a/nc-Si:H films deposited onto crystalline silicon substrates are shown in Figure 26 (these are from the same deposition runs as in Figure 25). The data are plotted in the range of 1800 to 2200 cm, showing the presence of the vibrational bond-stretching modes of Si-H at 2000 cm^{-1} and $Si-H_2$ at 2090 cm^{-1}. As described above, the microstructure fraction, defined as $R = I_{2090}/(I_{2090}+I_{2000})$ where I_{2000} is the area under the peak at 2000 cm^{-1} and I_{2090} is the area under the peak at 2090 cm^{-1} increases with nanocrystalline density in undoped a/nc-Si:H. The microstructure fraction determined by FTIR shows a similar increase in the doped a/nc-Si:H films with crystalline fraction X_c (as determined using Raman spectroscopy).
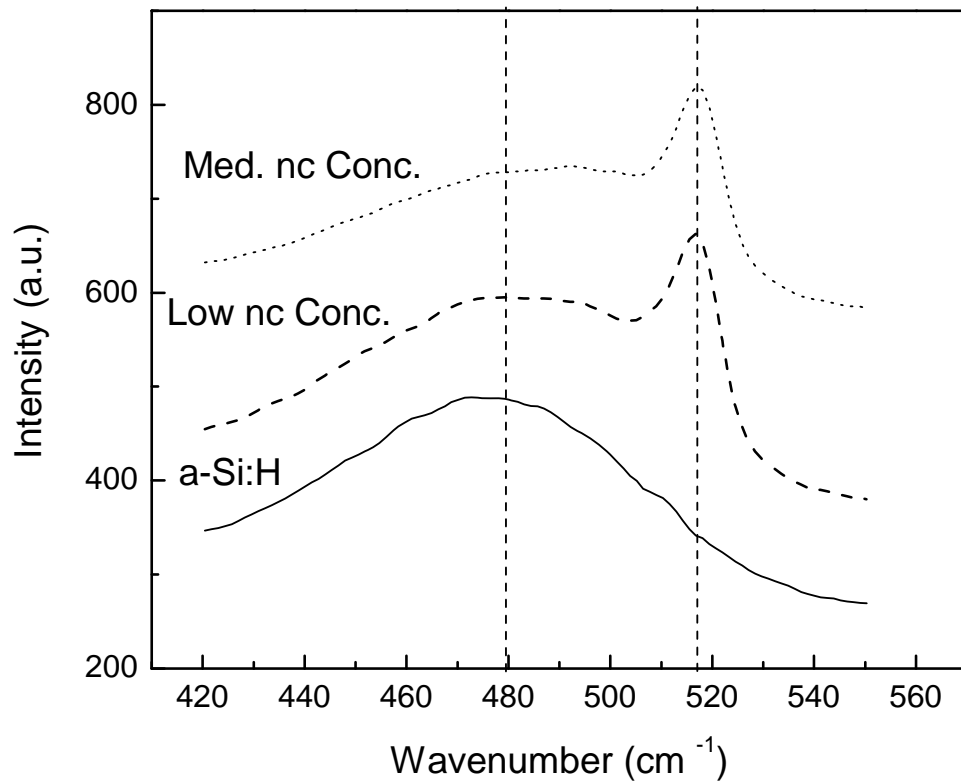
Figure 25: Plot of the Raman absorption spectra for 6 x 10^{-5} [PH$_3$]/[SiH$_4$] doped a/nc-Si:H films at various nanocrystalline concentrations. The curves are offset vertically for clarity.
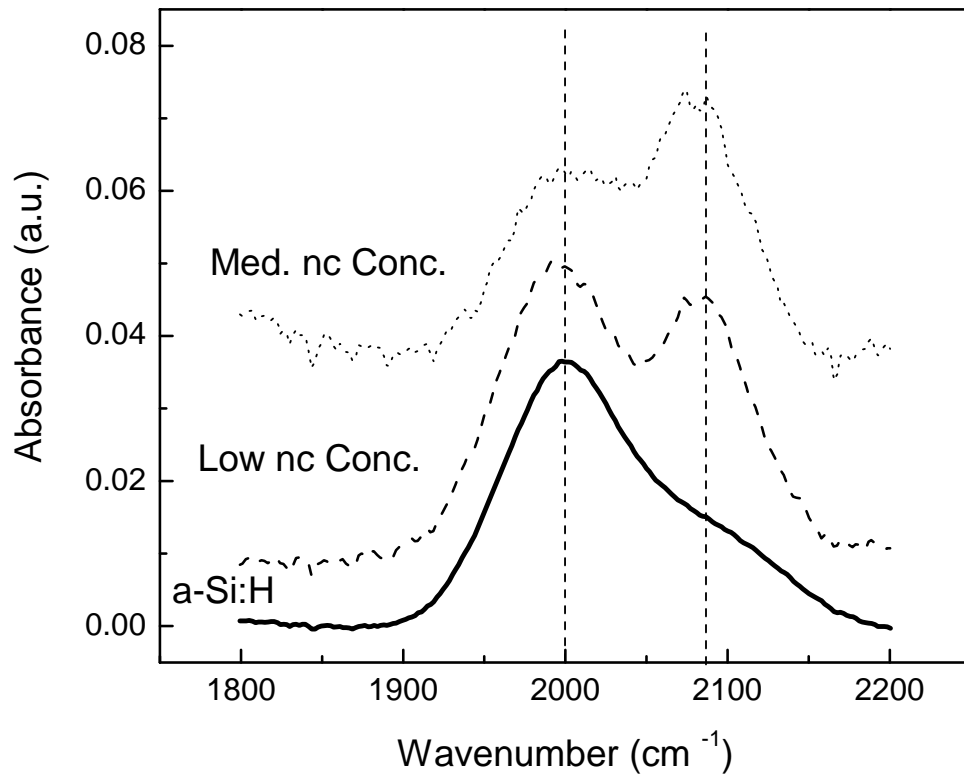
Figure 26: Infrared absorption spectra for 6 x 10^{-5} [PH$_3$]/[SiH$_4$] doped a/nc-Si:H films at various nanocrystalline concentrations. The curves are offset vertically for clarity.

The temperature dependence of the dark conductivity for these doped a/nc-Si:H films as a function of nanocrystalline concentration in the annealed state and following extended light exposure (the Staebler-Wronski effect) are shown in Figure 27. The conductivity of the films with the lowest nanocrystalline concentration overlapped with those with a moderate density of nanoparticle inclusions. These data have been omitted from Figure 27 for clarity. The films are first annealed at 450 K for 120 minutes under vacuum and then slowly cooled to 320 K. The conductance in the annealed state A is measured upon warming, at a rate of 3°/min (solid symbols in Figure 27). The addition of nanocrystals to the doped a-Si:H films results in lower dark conductivities and higher activation energies compared to n-type a-Si:H without nanoparticle inclusions.

Figure 27: Arrhenius plots of the dark conductivity of doped a/nc-Si:H films at various nanocrystalline concentrations, for (a) low doping (6 x 10^{-5} [PH$_3$]/[SiH$_4$]) and (b) high doping levels (6 x 10^{-3} [PH$_3$]/[SiH$_4$]). The filled symbols represent the dark conductivity in the annealed state A while the conductivity following extended light-soaking (state B) is represented by the open symbols.

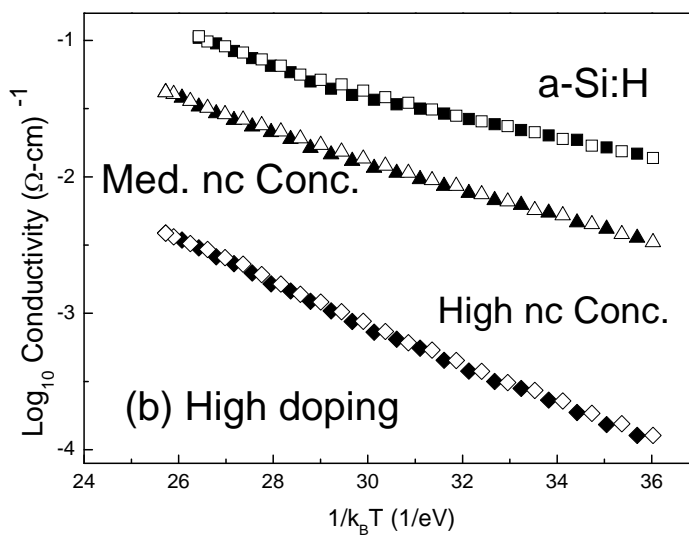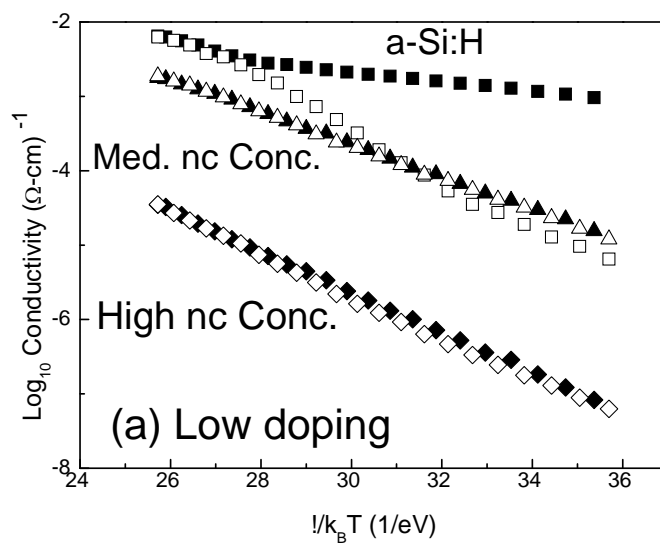| Doping level	Thickness (nm)	X_c % from RAMAN	Microstructure Fraction from FTIR	Activation Energy (eV)	Photoconductivity σ_{ph} $(\Omega \cdot cm)^{-1}$	Photosensitivity σ_{ph}/σ_a
Low	1210.0	0.0	0.30	0.181	1.7×10^{-3}	2.09
Low	590.9	9.6	0.42	0.349	1.7×10^{-4}	6.66
Low	240.2	11.9	0.54	0.500	5.6×10^{-5}	7.29
Low	73.3	29.7	0.70	0.623	2.6×10^{-6}	52.94
High	1186.7	0.0	0.37	0.204	1.6×10^{-2}	1.04
High	1114.0	0.4	0.52	0.235	4.0×10^{-3}	1.02
High	421.4	1.0	0.40	0.242	4.1×10^{-3}	1.12
High	117.8	3.2	1.00	0.347	2.6×10^{-4}	2.68

Table 2: Summary of the material and electronic properties for n-type doped a/nc-Si:H films. Films labeled as Low doping had a doping level of 6×10^{-5} [PH$_3$/SiH$_4$] while the films labeled as High doping had a doping level of 6×10^{-3} [PH$_3$/SiH$_4$].

The sample is re-cooled to 320 K and then light soaked (using a heat-filtered W-Ha lamp intensity ~ 100 mW/cm^2) for 22 hours. The State B conductivity is then measured upon warming (open symbols in Figure 27). The mixed phase n-type doped a/nc-Si:H films show no significant light induced degradation. The dark conductivity measured at 325K and activation energy obtained from the Arrhenius plots, as well as the photoconductivity and photosensitivity (defined at the ratio of the photoconductivity when illumination begins to the annealed state A dark conductivity) are summarized in Table 2. The addition of nanocrystalline inclusions leads to a more pronounced decrease

in the dark conductivity than the photoconductivity, such that the photosensitivity increases slightly for these films.

Studies of undoped a/nc-Si:H films synthesized in a dual chamber system similar to, but not identical to the one employed in this work have found that the addition of nanocrystalline inclusions leads to a non-monotonic increase in the dark conductivity, compared to pure a-Si:H films. That is, the highest conductance values are consistently observed in mixed phase thin films with a crystalline fraction of 2 – 4 %, as determined by Raman spectroscopy as in Figure 25, and even when the crystalline fraction is 10% or higher, the dark conductivity is greater than in films for which no nanocrystals are present. In contrast, for the doped a/nc-Si:H films reported here, the addition of nanocrystals always leads to a reduction in the dark conductivity. The increase in activation energy observed, particularly for the lightly doped films with the highest concentration of nanocrystals, is striking, as typically in doped a-Si:H the Fermi energy will not reside deeper in the mobility gap than the minimum in the density of states formed between the negatively charged dangling bond states and the conduction band tail, approximately 0.4 eV from the conduction band edge. It is likely that the larger activation energies observed here result from increased long-range disorder introduced by the nanocrystalline inclusions, which would have the effect of shifting the electronic transport level to higher energies, resulting in a larger conductivity activation energy.

Other doped mixed phase films were produced at greater gas pressures with the use of an orifice between the particle synthesis chamber and the amorphous silicon deposition chamber. The presence of crystalline particle inclusions were verified using micro-RAMAN spectroscopy. Imaging was also performed on some of these films to verify homogeneity of the particle distribution throughout the film. Images over an area of 15 micron x 15 micron were produced by acquiring RAMAN spectra at points on the sample 250 nm apart for a total of 3600 spectra. The integration time of the spectrum at each location was 0.25 s requiring ~15 minutes to produce a micrograph in addition to processing time and time required for the stage movement. Micrographs were created by defining filters for the 3600 spectra. Defining a filter centered around the 480 cm^{-1} peak of amorphous silicon, spectra with high a high intensity within the limits of the filter would appear as a bright pixel whereas spectra with a low intensity would appear as a dark pixel; another filter was defined to be centered around 514 cm^{-1} to detect nanocrystallites in the same manner.

By using the micro-RAMAN capabilities, we were able to detect agglomerations of nanoparticles in films, as seen in Figure 28. Thus it is indeed possible that the lower conductivity and higher activation energy in the doped films which contain higher crystalline fractions, as indicated by Raman spectra, also have larger agglomerates, possibly formed as the nanoparticles travel the length of the particle synthesis tube and enter the second plasma deposition chamber. By decreasing gas pressure in the particle chamber or by decreasing the conductance of the system by increasing the size of the

orifice, doped a/nc-Si:H films with a homogenous distribution of nanoparticle inclusions can be synthesized, as indicated in Figure 29.
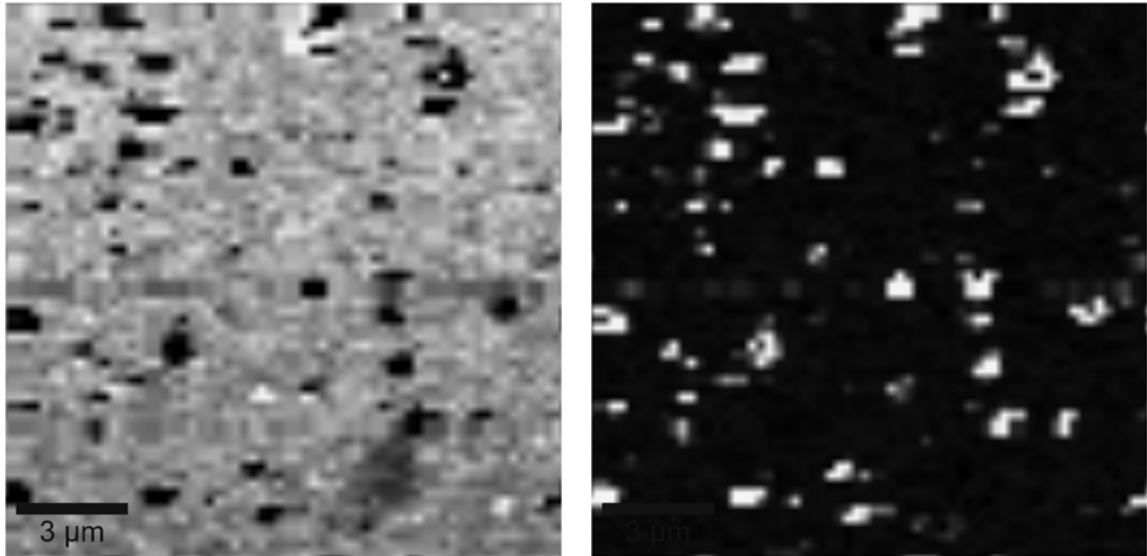
Figure 28. Using Micro-RAMAN Spectroscopy, detection of larger nanocrystallite agglomerations was possible. The micrograph on the left is filter for a-Si:H such that highly amorphous regions will appear as bright spots and the micrograph on the left is filtered for nanocrystalline particles so that high densities of nanocrystallites appear as bright regions. It is apparent by comparing the two micrographs that in the regions agglomerations are present there is a lack of a-Si:H in the same location.
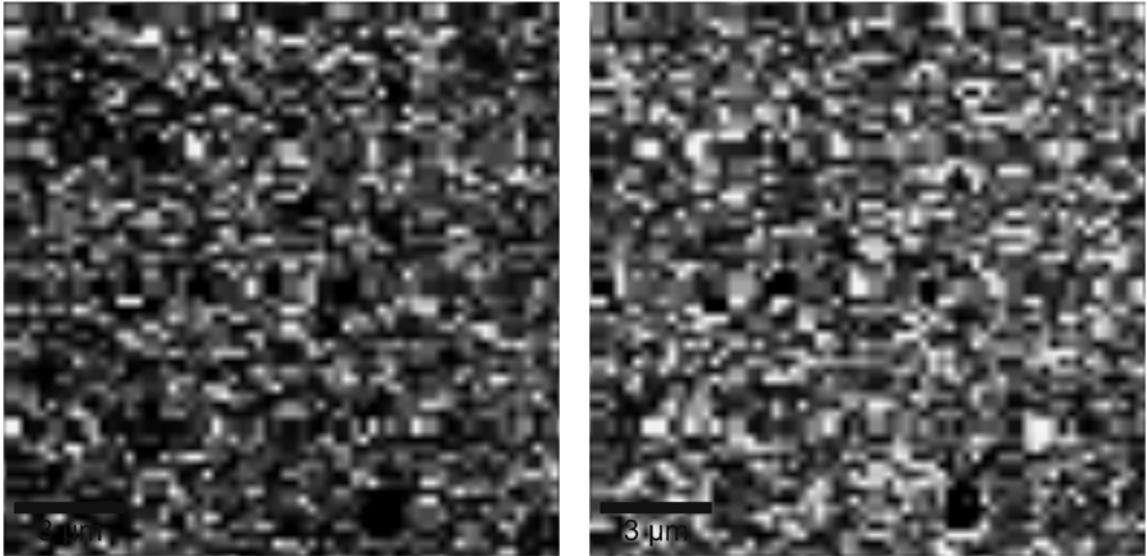
Figure 29. Using Micro-RAMAN Spectroscopy, detection of larger nanocrystallite agglomerations was possible. These micrographs show that there are not many highly crystalline regions with holes in the a-Si:H matrix; the film is homogeneous. The micrograph on the left is filter for a-Si:H such that highly amorphous regions will appear as bright spots and the micrograph on the left is filtered for nanocrystalline particles so that high densities of nanocrystallites appear as bright regions.

5.- Summary and Conclusions

We have investigated the influence of silicon nanocrystal concentration on the properties of mixed phase a/nc-Si:H thin films. When the mixed phase films are synthesized in a single PECVD chamber, the Staebler-Wronski effect decreased with the addition of nanocrystallites but with a concurrent decrease in the dark conductivity and photosensitivity. The density of silicon nanocrystals in the resulting a/nc-Si:H film was controlled by imposing a thermal gradient across the silane plasma during deposition. The drawback of this technique is that the conditions for silicon nanocrystallite formation are very far from those that optimize the opto-electronic properties of hydrogenated amorphous silicon. This motivated the work by the Kortshagen lab developing a dual chamber co-deposition PECVD system.

The mixed phase films synthesized in the dual chamber co-deposition system showed improved dark conductivities with the inclusion of nanocrystallites. Moreover, these films not only resisted light induced degradation, but some films grown with no thermal gradient across the silane plasma actually displayed a slight enhancement in the dark conductivity after extended light exposures. It was observed, as in the single chamber deposition system, that the dark conductivity of the films continued to change as the thermal gradient was varied in the system. The sensitivity of the a-Si:H matrix to the

thermophorectic force motivated a modification of the deposition system to employ a carrier gas to control the nanocrystal concentration in films.

The infra-red absorption spectra show a larger absorption at 2090 cm^{-1} with nanocrystal concentration. This is associated with hydrogen rich regions surrounding the nanocrystalline inclusions. It is possible that the surrounding amorphous silicon matrix is depleted of bonded hydrogen, compared to when a-Si:H is grown without nanocrystalline inclusions. In this way the a-Si:H matrix may be similar structurally to hot-wire deposited a-Si:H which has a low hydrogen content throughout bulk of the film, ~1%. Continued work is necessary to determine the optimum particle concentration of nanoparticles to yield films with the highest photoconductivities and greatest resistance to the Staebler-Wronski effect.

The influence of nanocrystal inclusions on doped mixed phase a/nc-Si:H has also been investigated. In contrast to the undoped a/nc-Si:H films, the addition of silicon nanocrystals reduces the dark conductivity for both low and high doping levels. More control is desired in the deposition of the doped mixed phase a-Si:H thin films. In other studies conducted with undoped mixed phase films it was observed that the introduction of nanocrystallites improved the quality of the film when the crystalline fraction was found to be around 4% by RAMAN characterization. The doped dual chamber deposition system is currently undergoing modification so that more precise control of the growth parameters is possible; the film precursor gases are no longer the residual

94

gases of the first chamber. With these modifications not only will nanocrystallites in a semiconductor matrix production be possible, but also nanocrystallites in an insulator matrix.

There is a striking reduction of the Staebler-Wronski effect in the lightly doped a/nc-Si:H films, with a silicon nanocrystalline concentration of roughly 10 at. %. It is well known that doped a-Si:H films contain significant potential fluctuations at the mobility edges, resulting from charged dopants and oppositely charged dangling bond defects. It is possible that this long-ranged disorder is enhanced by the inclusion of the nanocrystallites in these films, in essence increasing the barriers that an electrical current must overcome in order to transverse the distance between the co-planar electrodes. Studies comparing the activation energy obtained from Arrhenius plots of the dark conductivity to the temperature dependence of the open circuit Seebeck coefficient, which has been shown to be a measure of the long range disorder in a-Si:H, are presently underway in the Kakalios lab in order to address this issue.

References

1. A. Takano and T. Kamoshita, Japanese Journal of Applied Physics Part 1-Regular Papers Short Notes & Review Papers **43** (12), 7976-7983 (2004).
2. J. Yang, A. Banerjee and S. Guha, Solar Energy Materials and Solar Cells **78** (1-4), 597-612 (2003).
3. R. A. Street, Phys. Status Solidi A-Appl. Res. **166**, 695-705 (1998).
4. M. Schmidt, A. Schoepke, L. Korte, O. Milch and W. Fuhs, Journal of Non-Crystalline Solids **338**, 211-214 (2004).
5. R. Saleh and N. H. Nickel, Applied Surface Science **254** (2), 580-585 (2007).
6. D. Caputo, G. deCesare, F. Palma, M. Tucci, C. Minarini and E. Terzini, Thin Solid Films **303** (1-2), 269-272 (1997).
7. A. Reznik, S. D. Baranovskii, O. Rubel, G. Juska, S. O. Kasap, Y. Ohkawa, K. Tanioka and J. A. Rowlands, J. Appl. Phys. **102** (5) (2007).
8. B. N. Chapman, *Glow discharge processes : sputtering and plasma etching*. (Wiley, New York, 1980).
9. J. Mullerova, P. Sutta, G. van Elzakker, M. Zeman and M. Mikula, Applied Surface Science **254**, 3690-3695 (2008).
10. D. L. Staebler and C. R. Wronski, Applied Physics Letters **31** (4), 292-294 (1977).
11. D. Redfield, Applied Physics Letters **54** (4), 398-399 (1989).
12. S. B. Zhang and H. M. Branz, Phys. Rev. Lett. **87** (10), art. no.-105503 (2001).
13. A. H. Mahan, J. Carapella, B. P. Nelson, R. S. Crandall and I. Balberg, J. Appl. Phys. **69** (9), 6728-6730 (1991).
14. S. R. Jadkar, J. V. Sali, S. T. Kshrisagar and M. G. Takwale, Thin Solid Films **437** (1-2), 18-24 (2003).
15. B. Roy, A. H. Mahan, Q. Wang, R. Reed, D. W. Readey and D. S. Ginley, Thin Solid Films **516** (18), 6517-6523 (2008).
16. T. Unold, R. C. Reedy and A. H. Mahan, Journal of Non-Crystalline Solids **227**, 362-366 (1998).
17. Y. Lubianiker, J. D. Cohen, H. C. Jin and J. R. Abelson, Phys. Rev. B **60** (7), 4434-4437 (1999).
18. M. Meaudre, R. Meaudre, R. Butte, S. Vignoli, C. Longeaud, J. P. Kleider and P. R. I. Cabarrocas, J. Appl. Phys. **86** (2), 946-950 (1999).
19. R. Butte, R. Meaudre, M. Meaudre, S. Vignoli, C. Longeaud, J. P. Kleider and P. R. I. Cabarrocas, Philosophical Magazine B-Physics of Condensed Matter Statistical Mechanics Electronic Optical and Magnetic Properties **79** (7), 1079-1095 (1999).
20. C. R. Wronski, J. M. Pearce, R. J. Koval, X. Niu, A. S. Ferlauto, J. Koh and R. W. Collins, in *Materials Research Society Symposium* (715 A13.4.1, 2002).
21. K. Nishiguchi, X. Zhao and S. Oda, J. Appl. Phys. **92** (5), 2748-2757 (2002).

22. M. L. Ostraat, J. W. De Blauwe, M. L. Green, L. D. Bell, M. L. Brongersma, J. Casperson, R. C. Flagan and H. A. Atwater, Applied Physics Letters **79** (3), 433-435 (2001).

23. N. M. Park, T. S. Kim and S. J. Park, Applied Physics Letters **78** (17), 2575-2577 (2001).

24. P. R. I. Cabarrocas, A. F. I. Morral and Y. Poissant, Thin Solid Films **403**, 39-46 (2002).

25. B. C. Pan and R. Biswas, J. Appl. Phys. **96** (11), 6247-6252 (2004).

26. A. Hadjadj, A. Beorchia, P. R. Cabarrocas and L. Boufendi, Thin Solid Films **403**, 139-143 (2002).

27. C. Das, A. Dasgupta, S. C. Saha and S. Ray, J. Appl. Phys. **91** (11), 9401-9407 (2002).

28. E. A. G. Hamers, A. F. I. Morral, C. Niikura, R. Brenot and P. R. I. Cabarrocas, J. Appl. Phys. **88** (6), 3674-3688 (2000).

29. P. R. I. Cabarrocas, Journal of non-crystalline solids **266**, 31-37 (2000).

30. D. Kwon, C. C. Chen, J. D. Cohen, H. C. Jin, E. Hollar, I. Robertson and J. R. Abelson, Phys. Rev. B **60** (7), 4442-4445 (1999).

31. A. F. I. Morral and P. R. I. Cabarrocas, Thin Solid Films **383**, 161-164 (2001).

32. G. Viera, S. Huet, E. Bertran and L. Boufendi, J. Appl. Phys. **90** (8), 4272-4280 (2001).

33. R. Meaudre, M. Meaudre, R. Butte and S. Vignoli, Thin Solid Films **366** (1-2), 207-210 (2000).

34. S. Tchakarov, D. Das, O. Saadane, A. V. Kharchenko, V. Suendo, F. Kail and P. R. I. Cabarrocas, Journal of non-crystalline solids **338**, 668-672 (2004).

35. Y. Saito, M. Aomori and H. Kuwano, J. Appl. Phys. **81** (2), 754-757 (1997).

36. C. R. Wronski, J. M. Pearce, R. J. Koval, X. Niu, A. S. Ferlauto, J. Koh and R. W. Collins, Materials Research Society Symposium Proceedings **715**, 459 (2002).

37. Z. Shen, T. Kim, U. Kortshagen, P. H. McMurry and S. A. Campbell, J. Appl. Phys. **94** (4), 2277-2283 (2003).

38. Z. Shen, U. Kortshagen and S. A. Campbell, J. Appl. Phys. **96** (4), 2204-2209 (2004).

39. G. M. Jellum, J. E. Daugherty and D. B. Graves, J. Appl. Phys. **69** (10), 6923-6934 (1991).

40. S. Thompson, C. R. Perrey, C. B. Carter, T. J. Belich, J. Kakalios and U. Kortshagen, J. Appl. Phys. **97** (3) (2005).

41. A. Hadjadj, A. Beorchia, P. R. I. Cabarrocas, L. Boufendi, S. Huet and J. L. Bubendorff, J. Phys. D-Appl. Phys. **34** (5), 690-699 (2001).

42. D. Quicker and J. Kakalios, Phys. Rev. B **60** (4), 2449-2455 (1999).

43. C. Anderson, C. Blackwell, J. Deneen, C. B. Carter, J. Kakalios and U. Kortshagen, Materials Research Society Symposium Proceedings **910**, 79 (2006).

44. N. A. Fuchs, in *The Mechanics of Aerosols* (Dover, New York, 1964).

45. L. Mangolini, E. Thimsen and U. Kortshagen, Nano Letters **5** (4), 655-659 (2005).

46. U. Kortshagen, L. Mangolini and A. Bapat, J. Nanopart. Res. **9** (1), 39-52 (2007).

47. X. D. Pi, R. Gresback, R. W. Liptak, S. A. Campbell and U. Kortshagen, Applied Physics Letters **92** (25) (2008).
48. S. D. Walck and J. P. McCaffrey, Materials Research Society Symposium Proceedings **480**, 149-171 (1997).
49. D. B. Williams and C. B. Carter, in *Transmission Electron Microscopy* (Plenum, New York, 1996).
50. M. Tanielian, Philosophical Magazine B-Physics of Condensed Matter Statistical Mechanics Electronic Optical and Magnetic Properties **45** (4), 435-462 (1982).
51. D. L. Staebler and C. R. Wronski, J. Appl. Phys. **51** (6), 3262-3268 (1980).
52. G. Lucovsky, Journal of Non-Crystalline Solids **141** (1-3), 241-256 (1992).
53. M. H. Brodsky, M. Cardona and J. J. Cuomo, Phys. Rev. B **16** (Copyright (C) 2009 The American Physical Society), 3556 (1977).
54. G. Lucovsky, R. J. Nemanich and J. C. Knights, Phys. Rev. B **19** (4), 2064-2073 (1979).
55. E. Bhattacharya and A. H. Mahan, Applied Physics Letters **52** (19), 1587-1589 (1988).
56. D. C. Marra, E. A. Edelberg, R. L. Naone and E. S. Aydil, Journal of Vacuum Science & Technology a-Vacuum Surfaces and Films **16** (6), 3199-3210 (1998).
57. M. Vanecek, J. Kocka, J. Stuchlik and A. Triska, Solid State Communications **39** (11), 1199-1202 (1981).
58. P. Sladek, P. Stahel and M. L. Theye, Philosophical Magazine B-Physics of Condensed Matter Statistical Mechanics Electronic Optical and Magnetic Properties **71** (5), 871-880 (1995).
59. J. A. Schmidt and F. A. Rubinelli, J. Appl. Phys. **83** (1), 339-348 (1998).
60. S. K. J. Alani, Int. J. Electron. **75** (6), 1153-1163 (1993).
61. L. Escobar-Alarcon, A. Arrieta, E. Camps, S. Muhl, S. Rodil and E. Vigueras-Santiago, (unpublished).
62. E. Malainho, M. I. Vasilevskiy, P. Alpuim and S. A. Filonovich, J. Appl. Phys. **106** (7) (2009).
63. K. Tanaka and S. Nakayama, Jpn. J. Appl. Phys. Part 1 - Regul. Pap. Short Notes Rev. Pap. **38** (7A), 3986-3992 (1999).
64. K. Urban and M. Lentzen, Microscopy and Microanalysis **8**, 8 (2002).
65. A. Adikaari and S. R. P. Silva, J. Appl. Phys. **97** (11) (2005).
66. A. Hadjadj, J. L. Bubendorff, L. Boufendi and A. Beorchia, Applied Surface Science **208**, 272-276 (2003).
67. G. Viera, S. Huet and L. Boufendi, J. Appl. Phys. **90** (8), 4175-4183 (2001).
68. C. Min, Z. Weijia, W. Tianmin, J. Fei, L. Guohua and D. Kun, Vacuum **81**, 126 (2006).
69. R. Saleh and N. H. Nickel, Thin Solid Films **427**, 266-269 (2003).
70. C. Bohm and J. Perrin, J. Phys. D-Appl. Phys. **24** (6), 865-881 (1991).
71. A. Bouchoule, A. Plain, L. Boufendi, J. P. Blondeau and C. Laure, J. Appl. Phys. **70** (4), 1991-2000 (1991).

72.   J. Perrin, O. Leroy and M. C. Bordage, Contributions to Plasma Physics **36** (1), 3-49 (1996).
73.   C. R. Perrey, S. Thompson, M. Lentzen, U. Kortshagen and C. B. Carter, Journal of Non-Crystalline Solids **343** (1-3), 78-84 (2004).
74.   C. Blackwell, C. Anderson, J. Deneen, C. B. Carter, J. Kakalios and U. Kortshagen, Materials Research Society Symposium Proceedings **910** (2006).
75.   J. Kakalios and H. Fritzsche, Phys. Rev. Lett. **53** (16), 1602-1605 (1984).